Physics of Fluids

RESEARCH ARTICLE | AUGUST 14 2023

Influence of nozzle geometry on screech instability closure

A. Karnam ; M. Saleem ; E. Gutmark

Check for updates

Physics of Fluids 35, 086119 (2023)
https://doi.org/10.1063/5.0161032

View Online Export Citation

Articles You May Be Interested In

Screech characteristics of under-expanded high aspect ratio elliptic jet

Physics of Fluids (July 2020)

Experimental study of flight effects on screech in underexpanded jets

Physics of Fluids (December 2011)

Screech in transient supersonic jets

Physics of Fluids (September 2022)

17 March 2025 09:13:57

AIP Publishing

Physics of Fluids

Special Topics Open for Submissions

Learn More

AIP Publishing

Physics of Fluids ARTICLE pubs.aip.org/aip/pof

Influence of nozzle geometry on screech instability closure

Cite as: Phys. Fluids 35, 086119 (2023); doi: 10.1063/5.0161032
Submitted: 7 June 2023 · Accepted: 27 July 2023 ·
Published Online: 14 August 2023

View Online Export Citation CrossMark

A. Karnam,[a] M. Saleem, and E. Gutmark

AFFILIATIONS

Department of Aerospace Engineering and Engineering Mechanics, University of Cincinnati, Cincinnati, Ohio 45221, USA

[a]Author to whom correspondence should be addressed: karnamah@mail.uc.edu

ABSTRACT

The effect of nozzle exit geometry on the triadic interactions between convective Kelvin–Helmholtz instabilities and the quasi-steady shock structure of supersonic jets is discussed in this study. A circular and rectangular nozzle with an aspect ratio (AR) of 2 were evaluated using results from near field acoustics and high-speed Schlieren images. The study investigated different types of screech instabilities in both nozzle configurations, including the multimode instability in rectangular jets. The near field acoustic measurements showed comparable trends in screech staging in both nozzle configurations. The Schlieren results revealed that the standing waves in the jet near field were influenced by the oscillation mode of the jets. The study also explored a new technique of noise visualization from Schlieren images based on near field acoustics and temporal Fourier decomposition. Spatial Fourier decomposition demonstrated that the resonance closure mechanism across both nozzle configurations was dependent on the relative influence of the first two shock cells. Comparisons between the AR 2 and AR 9 jet showed that jet aspect ratio can significantly affect the energy distribution from the triadic interactions.

© 2023 Author(s). All article content, except where otherwise noted, is licensed under a Creative Commons Attribution (CC BY) license (http://creativecommons.org/licenses/by/4.0/). https://doi.org/10.1063/5.0161032

17 March 2025 09:13:57

I. INTRODUCTION

Supersonic jet screech is one of the most dynamic fields in aeroacoustic research due to the challenges associated with understanding, predicting, and suppressing this highly energetic flow phenomenon. Powell's[1,2] seminal studies detailing the observations of periodic oscillation in choked supersonic jets have since led to a large body of research that seeks to understand screech. While works by Tam,[3] Raman,[4,5] and Edgington-Mitchell[6] provide a comprehensive overview of the critical aspects of screech, ongoing developments in theorizing noise production and propagation mechanisms keep this field active. Tam and Tanna[7] and Tam *et al.*[8] through the "weakest link" model proposed that screech was a limiting case of the broadband shock noise (BBSN) and thus has to be directly influenced by the interactions occurring between the shock cells and coherent structures in the shear layers. The formulation for screech frequency (f_s) prediction resulting from these studies is shown in the following equation:

$$f_s = \frac{u_c k_n}{2\pi(1+M_c)}, \tag{1}$$

where u_c is the convective velocity of the coherent structures, M_c is the convective Mach number (u_c/a_0, where a_0 is the ambient speed of sound), and k_n is the spatial wavenumber ($k_n = 2\pi/\lambda_n$) associated with the nth shock cell ($n = 1, 2, 3, \ldots$). The key takeaway is that jet instability modes are closely tied to the interactions between the coherent structures (through their convective velocity u_c) and the shock cells (through the spatial wavenumber k_n) with the first shock cell ($n = 1$) having the greatest impact. Although the screech frequencies predicted from Eq. (1) closely matched the experimental results for circular nozzles, they could not quantify the frequency shift observed during the mode staging phenomena.[9,10] Panda's[11] study centered on the standing wave patterns[12] observed in screeching underexpanded circular jets from convergent nozzles led to similar formulation as shown in the following equation, where λ_{sw} is the wavelength of the standing wave:

$$f_s = \frac{u_c}{\lambda_{sw}(1+M_c)}. \tag{2}$$

This indicated that the periodic fluctuations resulting from screech led to the production of organized interference patterns between the upstream traveling acoustic waves and the downstream propagating hydrodynamic waves. These interactions occurring at the screech frequency can be realized in the spatial domain as shown in the following equation:

© Author(s) 2023

$$k_{sw} = k_s + k_h, \tag{3}$$

where k_{sw} is the spatial wavenumber of the standing waves ($k_{sw} = 2\pi/\lambda_{sw}$), k_s is the spatial wavenumber associated with the acoustic waves of wavelength λ_s ($k_s = 2\pi/\lambda_s$), and k_h is the spatial wavenumber associated with the hydrodynamic fluctuations of wavelength λ_h ($k_h = 2\pi/\lambda_h$) that are traveling with the convective velocity u_c. Thus, it can be inferred from these studies that along with temporal periodicity, screech instabilities demonstrate identifiable spatial characteristics associated with the oscillation frequency.

To elucidate the physics behind mode switching and multimode instability observed in circular jets, Shen and Tam,[13] based on the findings of Tam and Hu,[14] proposed that a neutral wave mode was the primary closure mechanism for the **A2** and **C** instability modes, while the acoustic feedback loop served as the closure mechanism for the **A1** and **B** modes. This neutral wave mode that is guided by the jet shear layer was referred to as the guided jet mode (G-JM) and offered a novel approach to comprehensively describe all instability modes. Building on the discoveries of Tanna,[15] recent research conducted by Edgington-Mitchell *et al.*[16–18] have provided insight into the mechanisms through which triadic interactions generate three distinct components: the acoustic emission, shock leakage phenomenon, and the guided jet mode (G-JM). These findings are particularly relevant for circular nozzles experiencing both conventional (single screech frequency) and multimode instability. Independent studies conducted by Mancinelli *et al.*[19] and Nogueira *et al.*[20,21] demonstrated that analyses incorporating the guided jet mode (G-JM) as the primary resonance closure mechanism produced results that closely matched experimental observations. Thus, these findings consolidate the notion that the G-JM, rather than the free stream acoustic mode, is the primary driver of the resonance mechanism. Numerical studies conducted by Bogey and Gojon[22] and Gojon *et al.*[23] also support this conclusion.

The concept of G-JM was found to be applicable in the case of the rectangular nozzles as shown by the experimental studies of Edgington-Mitchell *et al.*[24] In this study, high speed Schlieren imagery for elliptic and rectangular nozzles of aspect ratio (AR 2) were processed using spatial Fourier decomposition techniques to reveal the existence of G-JM by assessing the energy redistribution in the spatial domain resulting from the triadic interactions. The energy associated with specific wave numbers of these interactions was realized by the following equation:

$$k = k_{KH} \pm k_{Sn}, \tag{4}$$

where k_{KH} is the spatial wavenumber of the Kelvin–Helmholtz (*KH*) instability waves, and k_{Sn} is the spatial wavenumber of the *n*th shock cell. This formulation provides a method of isolating the effect of specific shock cells on triadic interactions. The study showed that in the case of the AR 2 rectangular jet, both the optimal shock peak (k_{S1}) as well as the suboptimal shock peak (k_{S2}) appeared to influence the production of G-JM. Similar evidence was also found by Gojon *et al.*[25] from numerical simulations conducted on the AR 2 rectangular jet. In contrast, previous studies[26–32] generally attribute the acoustic propagation to be the source driving the closure mechanism. A noteworthy observation is that the studies that established the connection between screech closure and the acoustic emission produced from screech flapping predominantly focused on nozzles with high aspect ratios (AR > 4), whereas the research by Edgington-Mitchell *et al.*[24] investigated nozzles with a lower aspect ratio. One question that arises is whether the AR of the nozzle influences the redistribution of energy in triadic interactions. In smaller AR nozzles, the weightage toward the acoustic emission, shock leakage, and G-JM appears to be similar, whereas larger AR nozzles seem to diminish the weightage of G-JM. Although the dominance of the flapping mode in rectangular jets was well-established, Suda *et al.*[33] presented evidence supporting the occurrence of both sinusoidal and varicose instability modes in these jets. Raman's[30] spectral analysis of rectangular nozzles (AR 5) revealed the presence of multimode instability. This behavior was also observed in AR 2 elliptical and rectangular jets by Edgington-Mitchell *et al.*[24] where interactions with the first shock cell was found to be the source of the main instability peak while the interaction with the second shock sourced the secondary instability peak. However, the effect of screech on spanwise fluctuations has not been thoroughly investigated.

In this study, the presence and effect of the G-JM is explored across two nozzle configurations—a circular and a rectangular nozzle (AR 2)—with both geometries based on an identical design condition. Additionally, the study explores the multimode behavior in the rectangular nozzle by analyzing its effect on shear layer development in both streamwise and spanwise directions. Furthermore, by comparing the two geometries, the effect of nozzle configuration on the triadic interaction is evaluated. Section I A provides a brief overview of the primary features of G-JM and discusses the terminology related to shock cell interactions.

A. Characteristics of G-JM

This section will introduce the conceptual formulation of wave interactions and provide an understanding of the terminology. In order to separate the individual components of triadic interactions, such as acoustic waves, *KH* instability waves, and neutral G-JM waves, it is useful to examine the energy distribution associated with the screech frequency [such as the dominant modes from proper orthogonal decomposition (POD)] and decompose it into spatial components. This associates the component waves and their interactions with deterministic values. For any given wave, the relationship between wave propagation velocity (u_p) and spatial wavelength (λ) is given by the following equation from Tam and Tanna:[7]

$$k = \omega/u_p, \tag{5}$$

where k is the spatial wavenumber ($k = 2\pi/\lambda$), and ω is the angular frequency. The waves in the spatial domain propagate in both upstream and downstream directions. Therefore, a positive sign ($+u_p$) is assigned to the downstream phase velocities, and a negative sign ($-u_p$) is assigned to the upstream velocities. It is clear from Eq. (5) that this convention extends to the wavenumbers. Towne *et al.*[34] demonstrated that the dispersion relation of *KH* instability waves has a linear relationship in the frequency–wavenumber spectra, implying that the observed phase velocity (u_p) is equivalent to the group velocity ($\partial\omega/\partial k$) of these wave packets. Therefore, the sign of the phase velocity (and thus the wavenumber) can indicate the sign of the group velocity at any given frequency,[17] facilitating the identification of the direction of propagation of different wave components.

As stated earlier, the energy distribution associated with the interaction wavenumbers is given by Eq. (4), where k_{Sn} represents the wavenumber associated with the *n*th shock cell ($n = 1, 2, 3, \ldots$).

17 March 2025 09:13:57

© Author(s) 2023

Fully resolving the interaction between all shock cells necessitates an infinite spatial domain, which is impractical. The strength of the shock system reduces as the distance from the nozzle exit increases due to core velocity variation. As a result, the influence of weaker shock cells on the interaction with *KH* wave packets decreases. Edgington-Mitchell *et al.*[17] and Nogueira *et al.*[20] concluded that the condition for absolute instability, which allows a spatially periodic base flow to develop continuous oscillatory behavior, the wave interactions given by Eq. (5) must satisfy the following condition:

$$k_g = k_{KH} - k_{Sn}, \tag{6}$$

where k_g is the wavenumber associated with resultant of the interaction which, in the current context, is the guided jet mode. Based on this formulation, Nogueira *et al.*[20] elaborated on the mode staging behavior by showing that the **A1** mode was associated with the interaction of the *KH* wave packet with the first shock ($k_{KH} - k_{S1}$), while the **A2** mode was associated with the second shock ($k_{KH} - k_{S2}$). Subsequently, Edgington-Mitchell *et al.*[16] found that in circular jets, the G-JM production in the antisymmetric **B** mode of oscillation was impacted by the first shock cell (k_{S1}), whereas the suboptimal shock cells (k_{S2}, k_{S3}) had a greater effect on multimode instabilities.

The guided jet mode (G-JM) displays two notable characteristics. First, the velocity of wave propagation associated with this mode is lower than the ambient speed of sound.[13] Second, the energy intensity of these neutral waves is primarily concentrated in regions near the shear layers, exhibiting a sharp decline in intensity at large radial distances from the lip line (referred to as evanescent waves). In contrast, the energy of acoustic waves (k_a) shows a gradual decrease in intensity across distances of up to two nozzle diameters in the radial direction.

II. EXPERIMENTAL AND ANALYSIS TECHNIQUES

A. Nozzle geometry and near field acoustics

Both nozzles were of convergent–divergent type with a sharp throat and a design Mach number (M_d) = 1.5 to replicate high-performance aircraft nozzles. The choice of identical design condition was made so as to isolate the effect of nozzle geometry on flow development. The rectangular nozzle profile was chosen due to its advantages in improved airframe integration,[35] higher mixing, and reduced noise levels[36] when compared to identical circular geometries.

Figure 1 shows the geometry and microphone layout used for each nozzle's near-field acoustic tests, along with the observation planes for the rectangular nozzle. The origin of the reference axes was located at the nozzle geometric center (flow direction: X_+). The circular nozzle has an exit diameter (D_e) of 20.66 mm, while the rectangular nozzle has exit dimensions of 12.95 mm (h_j), 25.9 mm (b_j), resulting in an AR of 2. The parameters of the rectangular nozzle were chosen to have the same pressure drop as the circular, resulting in an equivalent diameter [defined as $D_e = 1.30(b \cdot h)^{0.625}/(b+h)^{0.25}$, h: height, b: breadth] of 20.66 mm. Hence, the equivalent diameter (D_e) was utilized as the normalizing factor. Tests were conducted in the heated jet noise rig (HJNR) located in the Gas Dynamics and Propulsion Lab at the University of Cincinnati.[37] In the present study, the inlet flow temperature was maintained at ambient conditions, while the nozzle pressure ratios (NPR = P_{total}/P_{amb}) covered the overexpanded regime

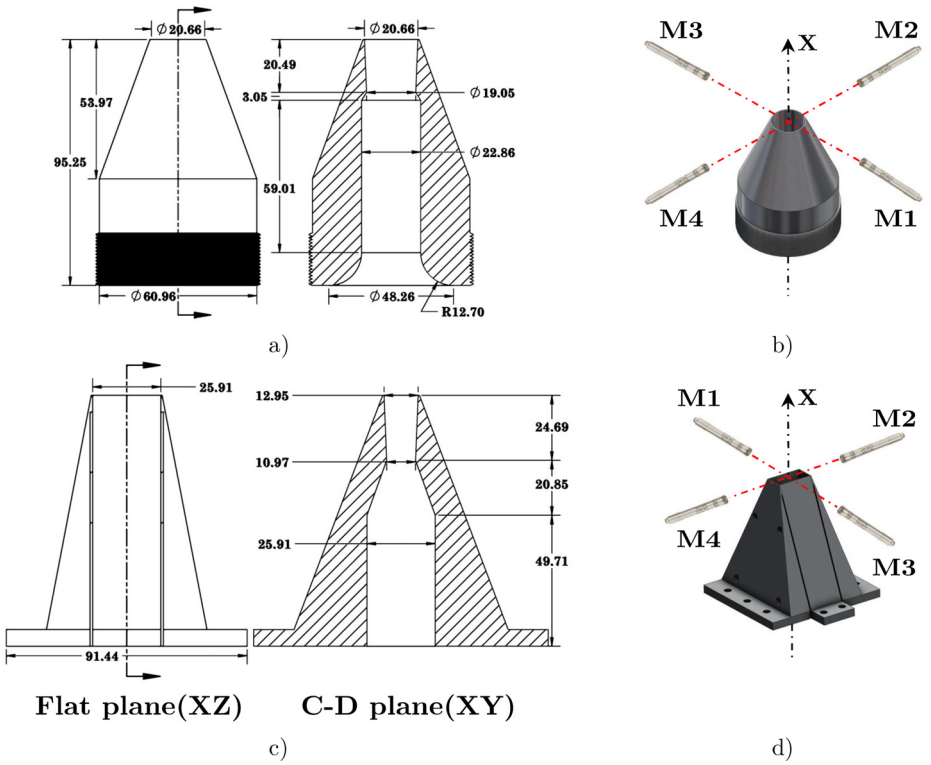


FIG. 1. Nozzle geometry and near field microphone set up: (a) dimensions and sectional view of the circular C–D nozzle, (b) near field array, microphone axial location: nozzle exit plane, (c) dimensions and orientation planes for the rectangular AR-2 nozzle, and (d) near field array: two microphones in each orientation plane. Axial location: nozzle exit plane. Design Mach number = 1.5, design pressure ratio = 3.67 for both nozzles.

17 March 2025 09:13:57

© Author(s) 2023

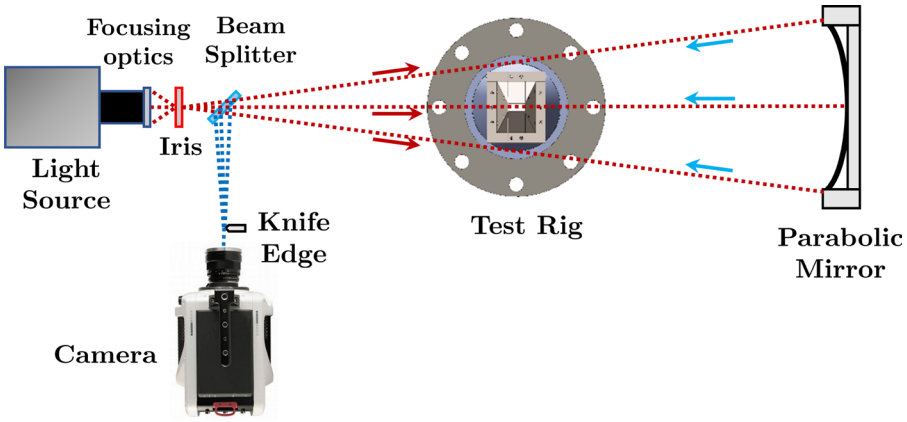


FIG. 2. Single mirror Schlieren setup. Red arrows represent the emanating rays from the light source, and the blue arrows represent the reflected rays bouncing off the mirror. Lengths not to scale.

(NPR 2.5 to NPR 3.67 at 0.1 increments), which is the unstable flow regime for both nozzles. Microphones were strategically arranged in the nozzle exit plane (X = 0), as seen in Fig. 1, to capture acoustic data. The centerline distance to the microphone was 45 and 100 mm for the rectangular and circular nozzles, respectively.

Acoustic data were acquired using Brüel and Kjaer 0.25 in. microphones in the free-field mode over a period of 2 s (acquisition rate = 204 800 Hz). Despite not being fully anechoic, the nozzle installation was padded with sound-absorbent foam to prevent signal interference through reflections (for acoustic testing). The data were processed using a fast Fourier transform (FFT) block averaging algorithm over 100 blocks with 4096 samples/block, resulting in a frequency resolution of 50 Hz. The standard reference of 20 μPa was utilized for sound pressure level (SPL) computation.

B. Schlieren imaging

A single mirror coincident system[38] was chosen due to the space constraints imposed by the geometry of the facility. Figure 2 shows a schematic of the optical arrangement. Flow was illuminated with an Oriel UV arc lamp (100 W, constant luminance) with focusing and confining optics to simulate a point source of light located at the 2f point of a first surface parabolic mirror (focal length f = 1828.8 mm). The light path goes through a beam splitter, measurement domain, and back to the beam splitter before reaching the camera. Precise optical alignment eliminated image doubling, a common artifact in single mirror configurations. Images were acquired using a Phantom v1610 paired with a Sigma f3 70–300 mm lens at two acquisition rates, 45 (circular nozzle) and 41 kHz (rectangular nozzle). This variation in acquisition rates was accounted for in the analyses. For testing, the lens was set to f4 at 300 mm with an exposure time of 10 μs. A higher exposure time was used to compensate for the reduction in light intensity due to the beam splitter and was found to not affect the quality of the results. LaVision Davis 8.4 was used for image acquisition with spatial calibration to account for magnification effects. The resulting domain spanned $8 \times 6D_e$ (axial $\times$ radial) with a spatial resolution of $0.15D_e$. The conditions under consideration are shown in Table I. Schlieren images capture only quasi-2D behavior due to line of sight integration of the first density gradient. However, LESs (large eddy simulations) conducted by Viswanath *et al.*[36] and Gojon *et al.*[25] on the current geometries did not report any spanwise shock cell deviations that could alter the jet behavior.

C. Schlieren image analysis

1. Temporal decomposition

Of the two analyses conducted on the Schlieren images, the first was temporal frequency decomposition. This technique is based on the study by Mercier *et al.*[39] for processing images but has been substantially modified. The luminance level of Schlieren images represents the first spatial gradient of refractive index ($\partial n/\partial z_n$—refractive index, z_n—axis parallel to light path), which is sensitive to the local density of the medium. From the equation of state, the light intensity gradients are also correlated with the temperate and pressure in the non-vortical regions of the jet. To establish a correlation between the noise levels (pressure field fluctuations) in the near field and the intensity variations in the Schlieren images, a simplistic scaling factor is proposed that equates the overall sound pressure level (OASPL) to an integral energy term obtained from the temporal Fourier space of the Schlieren results. This was achieved as follows: an algorithm performed a fast Fourier transform (FFT) in the time domain across all spatial locations transforming the temporal intensity variation (I) into the frequency domain as shown in the following equation:

$$I(x, y, t) = \sum_{\omega} \hat{I}_{\omega} e^{-i\omega t}, \tag{7}$$

where $I(x, y, t)$ is the local intensity fluctuation in a snapshot, and the right hand term is the temporal Fourier component that contains the energy (real part) and phase (imaginary part) information at a given frequency ω. To maintain a consistent frequency resolution (50 Hz), the FFT block size was adjusted accordingly ($N_{B,\ Circular}$: 900 images;

TABLE I. Test conditions for Schlieren.

NPR	Mach no.	Exit velocity (m/s)	Reynolds no.
2.5	1.22	371	6.8×10^5
2.6	1.25	378	7.1×10^5
3	1.36	401	8.5×10^5

17 March 2025 09:13:57

© Author(s) 2023

$N_{B,\ Rectangular}$: 820 images) with an overlap of 50% between blocks. This allowed for comparable frequency scaling between flow and noise results. The energy distribution for each frequency, termed as the resolved intensity (ζ_i), was computed as follows:

$$\zeta_i = 20log_{10}\frac{|\hat{I}_\omega|}{I_{ref}}, \tag{8}$$

$$Z = \sum \zeta_i, \tag{9}$$

$$\eta_s = \frac{Z}{OASPL_{ac}}\bar{I}_{Bi}, \tag{10}$$

$$I_{ref} = P_{ref} \times \eta_s. \tag{11}$$

The algorithm commenced at a reference point, using an initial estimate for the reference intensity (I_{ref}) from Eq. (8) to calculate the resolved intensity (ζ_i) across all frequencies (ω). These values were integrated to compute the cumulative energy levels and determine the integral energy (Z) in Eq. (9). This term was utilized to determine a scaling parameter (η_s) in Eq. (10), which is a function of the integral energy, acoustic OASPL at the reference location, and the average background intensity ($\bar{I}_{Bi}$). An iterative process then updated the reference intensity using the scaling parameter as shown in Eq. (11), where P_{ref} is the reference acoustic pressure (20 μPa). The reference location corresponds to the microphone location **M1** in Fig. 1. Once the scaling factor was determined, it was applied to the entire spatial domain to generate a distribution of ζ_i.

Although the resolved intensity (ζ_i) values are by no means an accurate depiction of the near field acoustics (or internal acoustic patterns) surrounding these nozzles, they bear striking qualitative resemblance to spatial spectral distribution similar to the numerical results obtained from pressure fields by Gojon *et al.*[23] in their study of underexpanded screeching circular jets. Since the phase patterns generated from the temporal decomposition were not subject to the processing described above, they accurately represent the resultant phase at each frequency. The reader must bear in mind that this is a preliminary exercise in visualization and is aimed at providing additional utility to Schlieren images. With the simple addition of a microphone in the flow domain, this method can be utilized as a qualitative tool to understand the effect of flow fluctuations on the local energy distribution and the resulting acoustical emissions.

2. Spatial decomposition

To isolate the various spatial components coupled with the instability tones of the nozzles, a spatial decomposition algorithm based on the work of Edgington-Mitchell *et al.*[16,17] was implemented. While their studies used the dominant modes from POD and dynamic mode decomposition (DMD) of screeching jets, respectively, in the current study, the results of the temporal Fourier decomposition at the screech frequency were used as an input for the algorithm as shown in the following equation:

$$\psi = \hat{I}_\omega\, e^{-i\omega t}, \tag{12}$$

$$\hat{\psi}_k^\omega(y) = \sum \psi(x,y)e^{-ikx}, \tag{13}$$

where ψ is the temporal Fourier term associated with the frequency of interest (ω), and $\hat{\psi}_k^\omega(y)$ is the streamwise spatial Fourier transform computed at each radial location converting the energy distribution from the spatial-frequency domain into the spatial-wavenumber domain. As discussed in Sec. I A, the positive wavenumbers identify waves propagating in the downstream direction, while the negative wavenumbers identify those traveling toward the jet upstream. Similar analysis was performed along the centerline of the temporal average of the Schlieren images to extract the spatial wavenumber associated with the shock cell structure of the jet. This method is input agnostic and can easily be adapted to process other energy modes.[24] While POD was explored as a potential technique to extract energetic flow features from Schlieren images, as shown by Berry *et al.*,[40] the temporal decomposition method utilized in this study was deemed to be a more comprehensive approach due to its ability to associate all fluctuation scales at a specific frequency.

III. RESULTS

The results obtained from the experimental techniques are discussed in the following order. First, the near field acoustics results are examined to identify trends in instability tones. Second, flow features are characterized through the high-speed Schlieren images. Finally, the sources driving screech induced jet oscillations are understood through the results of the temporal and spatial Fourier analyses.

A. Acoustics: Near field

Since the microphones were positioned at different distances from the nozzle centerline ($d_C = 100$ mm; $d_R = 45$ mm), the recorded noise levels do not provide a direct comparison between the two nozzle configurations. However, the trends in instability frequencies can be compared between the two as they are independent of the observer position. Figure 3 shows the NPR vs Strouhal number (St) spectra for both nozzles with markers indicating instability tones. The abscissa spans from NPR 2.5 to NPR 3.67(design) at 0.1 NPR increments, and the Strouhal number on the ordinate was computed using the equivalent diameter ($St = f \cdot D_e/U_j$, f—*frequency in Hz*).

In the case of the circular nozzle, no screech peaks were detected for the conditions of NPR 2.5 and NPR 2.6, as seen in Fig. 3(a). Instead, the noise peaks at these NPRs appeared in the broad-band shock associated noise (BBSN) region ($St_{range} \approx 0.55$–1.1; 10–20 kHz). However, a consistent screech peak was observed in the far field spectra (see Appendix A), indicating the screech tones at these NPRs propagated at very shallow azimuthal angles. Distinct screech tones and their respective harmonics were observed in the spectrum between the conditions of NPR 2.7 and NPR 3.4. The jet oscillation mode was found to be in the antisymmetric/sinusoidal **B** mode ($m = 1$) for these conditions resulting in noise peaks that were 15–30 dB above adjacent frequencies (± 100 Hz) and occurred well before the BBSN frequency range. Screech frequencies trended toward lower values as the NPR approached the design condition.

Studies[26–31,41,42] have demonstrated that rectangular jets exhibit variations in their noise intensity and directivity patterns depending on the orientation of the nozzle and observer position. Typically, turbulence and instability noise levels were higher when the observer was located perpendicular to the larger dimension of the jet. In the current study, this plane is referred to as the C–D plane (XY) with microphone **M1** located in this plane with the corresponding spectral contour shown in Fig. 3(b). The contour showed several high-intensity tones, with screech frequencies trending toward lower values with increase in NPR, resulting from the higher initial shock cell width.[8] This trend was consistent with the observations for the circular nozzle. The peak

17 March 2025 09:13:57

© Author(s) 2023

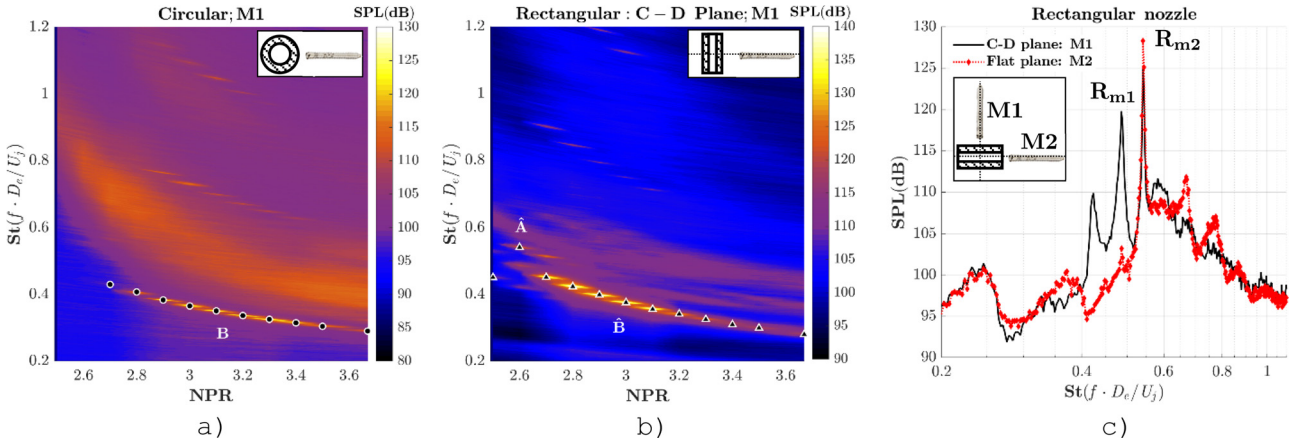


FIG. 3. Near field acoustics: NPR vs St contours, markers show peak frequencies: (a) circular nozzle (inset: microphone—**M1**), (b) rectangular nozzle: C–D plane (inset: microphone—**M1**), and (c) rectangular nozzle frequency spectra: **M1** (black) and **M2** (red) (inset: microphone orientation). Note that contour limits vary.

noise value for the rectangular nozzle was recorded at NPR 2.8 compared to NPR 3.3 for the circular jet. Phase analysis indicated a strong antisymmetric jet flapping in the C–D plane (XY) starting at NPR 2.7 (indicated as $\hat{\mathbf{B}}$ mode).

At NPR 2.6, multiple screech peaks were detected in the acoustics data for the rectangular nozzle [indicated by $\hat{\mathbf{A}}$ in Fig. 3(b)] with the associated frequency spectra shown in Fig. 3(c). The following observations were drawn from the spectral plot. Multimode oscillations were detected at this condition that led to the production of two screech frequencies, one at $\mathrm{St} \approx 0.5(9100\,\mathrm{Hz})$, designated as $\mathbf{R_{m1}}$, and another at $\mathrm{St} \approx 0.54(9900\,\mathrm{Hz})$, designated as $\mathbf{R_{m2}}$. A third low intensity peak at $\mathrm{St} \approx 0.43(7850\,\mathrm{Hz})$ was also observed but did not exhibit a consistent phase pattern. While $\mathbf{R_{m2}}$ was the dominant frequency in both nozzle orientations, $\mathbf{R_{m1}}$ was detected only in the C–D plane (XY). Furthermore, the results from phase analysis (see Appendix B) showed that the jet oscillated in the antisymmetric mode at $\mathbf{R_{m1}}$ and in the symmetric mode at $\mathbf{R_{m2}}$. To assess the impact of the coupled instability mode, a comparison between the experimental results and Tam's[8,27] screech prediction model was conducted for both nozzle configurations.

For circular jets, the screech frequency (f_s) of a cold jet ($T_{inlet} = T_{ambient}$) was computed as

$$\frac{f_s D_j}{U_j} \cong 0.67\left(M_j^2 - 1\right)^{-\frac{1}{2}}\left[1 + u_c M_j\left(1 + \frac{\gamma - 1}{2}M_j^2\right)^{-\frac{1}{2}}\right]^{-1}, \quad (14)$$

where D_j is the fully expanded jet diameter,[8] M_j is the fully expanded Mach number, U_j is the exit velocity, and u_c is the convective velocity. For rectangular jets, the screech frequency prediction is as follows:

$$\frac{f_s h}{U_j} = \frac{\dfrac{u_c/U_j}{2(1 + u_c/c_\infty)\left(M_j^2 - 1\right)^{\frac{1}{2}}}\left[\left(\dfrac{h_e}{b_e}\right)^2 + 1\right]^{\frac{1}{2}}}{\left\{\left[\left(\dfrac{1 + \frac{\gamma-1}{2}M_j^2}{1 + \frac{\gamma-1}{2}M_d^2}\right)^{\frac{(\gamma+1)}{2(\gamma-1)}}\dfrac{M_d}{M_j} - 1\right]\dfrac{b}{b+h} + 1\right\}}, \quad (15)$$

where M_d is the design Mach number of the nozzle, h_e and b_e are the fully expanded jet dimensions,[27] and h and b are the geometric dimensions at the exit. The convective velocity for both cases was assumed as $u_c \approx 0.7U_j$. The reader must bear in mind that Eqs. (14) and (15) were computed for purely convergent nozzles. The resulting comparison between predictions and the experimental data is shown in Fig. 4. Note that the frequencies marked for the circular nozzle at NPR 2.5 and NPR 2.6 were identified from far field acoustics.

For the circular nozzle, values from Eq. (14) closely followed the trend of the experimental results with slight overprediction. The screech tones recorded for NPRs 2.5 and 2.6 were notable exceptions. Further discussion on these two conditions is provided in Sec. III C as part of the Schlieren analysis. As the NPR approached the design condition, the deviation between the predicted and experimental frequencies in the **B** mode decreased. Similarly, for the rectangular nozzle, experimental values showed considerable deviation at lower pressure ratios but trended closer to the values from Eq. (15) near the design condition of NPR 3.67. However, at NPR 2.6, the dominant frequency $\mathbf{R_{m2}}$ that led to symmetric jet oscillation was a notable exception to this trend. This deviation at lower pressure ratios was due to the manifestation of multiple suboptimal instability modes at these conditions. This suggests that the measured screech frequency would coincide

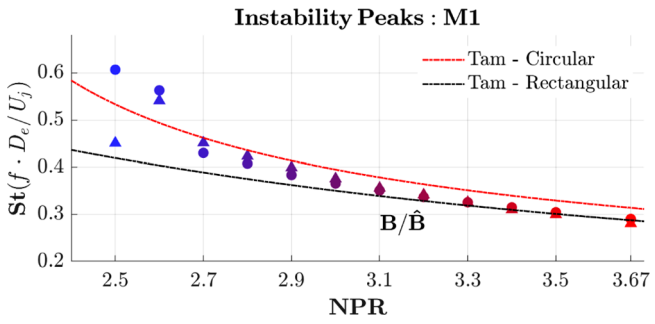


FIG. 4. Experimental screech frequencies (St) compared to Tam's model. Colors (online) indicate the operating condition. **B**/$\hat{\mathbf{B}}$: sinusoidal mode for the circular/rectangular nozzle. Filled circle—circular nozzle; filled triangle—rectangular nozzle.

17 March 2025 09:13:57

© Author(s) 2023

with the prediction at conditions where the dominant jet oscillation mode is purely antisymmetric, as in the case of NPR 3.4 at St ≈ 0.31(6400 Hz). Interestingly, the screech frequencies were remarkably similar across both nozzles in the antisymmetric mode ($m = 1$). The level of deviation from formulation observed here is not unexpected as documented in the studies by Liu *et al.*[43] and Jeun *et al.*[44] for circular and rectangular nozzles, respectively.

Spectrograms using a short-time Fourier transform algorithm were computed from the pressure data of microphones **M1**, **M2** for the rectangular nozzle at the condition of NPR 2.6 to further examine the coupled instability mode. These contours, shown in Fig. 5, provide the temporal variation in the frequency levels as opposed to the temporal average in Fig. 3(c). The continuous production of both instability tones is clear from Fig. 5(a), with $\mathbf{R_{m2}}$ consistently higher in magnitude in the C–D plane (XY) of the jet when compared to $\mathbf{R_{m1}}$. In the flat plane (XZ), the lower frequency tone $\mathbf{R_{m1}}$ had a drastically reduced magnitude, while $\mathbf{R_{m2}}$ dominated the spectra throughout the signal duration as seen in Fig. 5(b). This pattern is reminiscent of the observations of Raman[30] for high AR nozzles and demonstrates the continuous production of the coupled instability without mode switching/hysterisys.[9]

Although the multimode jet oscillation has been studied in both circular[16,45] and rectangular jets,[24,30] there is a lack of discussion regarding the influence of nozzle geometry and AR on screech instability production and its impact on spanwise deviations. The acoustic results obtained from the current study suggest that low AR can contribute to the generation of coupled symmetric and antisymmetric oscillations in rectangular jets that affect both nozzle orientations. In Sec. III B, the results of Schlieren image analysis exploring the spatial features resulting from these flow instabilities are discussed.

B. Schlieren: Average metrics and flow features

High-speed Schlieren images were recorded with the knife edge positioned normal to the flow direction to increase the contrast in the shock-expansion zones and emphasize the acoustic propagation. This resulted in shocks appearing as regions of high light intensity while expansions appeared as regions of low intensity. To investigate the evolution of the internal shock system, the temporal average of the Schlieren images at various NPRs was examined as shown in Fig. 6. The columns of the figure represent each NPR, while the rows are organized according to the nozzle configuration. The underexpanded condition of NPR 5 is included only in this section to provide a comprehensive overview of shock cell development.

For the overexpanded condition of NPR 2.5, a Mach disk was detected at $X/D_e = 0.18$ from the nozzle exit for the circular jet, followed by a shock train with decreasing axial cell width downstream, as seen in Fig. 6(a). At the same condition, the rectangular jet in the flat plane (XZ) also showed the formation of a Mach stem at $X/D_e = 0.15$ from the nozzle exit, with visible slip lines emanating from the stem on either side of the centerline in the C–D plane (XY), as seen in Figs. 6(e) and 6(i). At the screeching case of NPR 3, the Mach disk radius diminished significantly in the circular jet while forming further away from the nozzle exit at $X/D_e = 0.33$, as seen in Fig. 6(b). Reduced shock cell definition was observed for $X/D_e > 4.5$ due to the sinusoidal flapping of the jet induced by screech.

The secondary shock system that emerges from the sharp conical throat was also observed. In contrast, the Mach stem of the rectangular jet was not visible in the flat plane (XZ), as seen in Fig. 6(f). Similar loss of shock definition was observed after $X/D_e = 4$ due to the flapping of the jet. This phenomenon was more pronounced in the C–D plane (XY) along with the visible throat shock system, as seen in Fig. 6(j). The twin shock system was most prominent at the design condition of NPR 3.67, especially for the circular jet, as depicted in Fig. 6(c). This can be attributed to the relatively weak exit shock system as the nozzle is ideally expanded at this condition. The rectangular jet also showed a weak exit shock system when viewed from both orientations, as seen in Figs. 6(g) and 6(k).

Finally, for the highly underexpanded case of NPR 5, the shock train initiated with an expansion fan at the nozzle exit for pressure equalization, as the exit pressure was higher compared to ambient as seen in Figs. 6(d), 6(h), and 6(l). Due to the improper expansion, the jet exit dimensions across all configurations were larger than the geometric values. Also evident was a significant increase in the shock cell width. The average shock cell width has been frequently used in the literature to quantify the development of the internal shock train. It is computed by measuring the distance between shock/expansion inflection points on the jet shear layer.[11,46] This exercise was quite straightforward for the circular nozzle at the lower NPRs and was computed by correlating the intensity gradient along the jet shear layer and centerline.

However, at the design condition, the secondary shock train generated from the throat made it difficult to accurately identify the inflection points of the exit shocks. This problem is compounded in the case of the rectangular nozzle due to shock–shock interactions.[47]

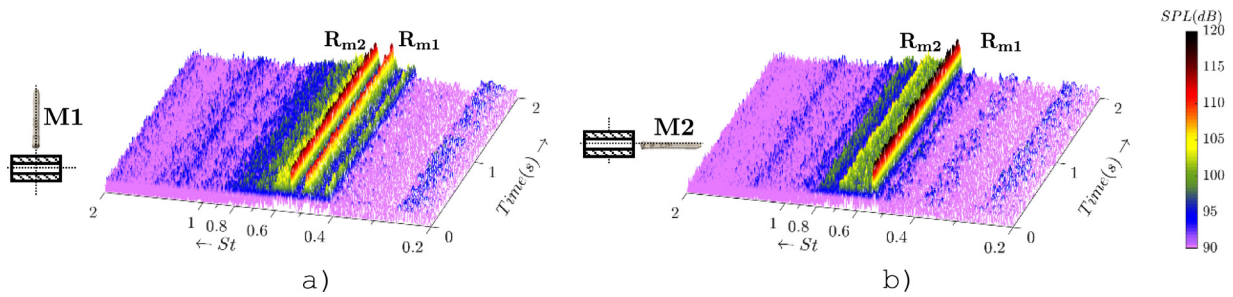


FIG. 5. Spectrogram of St vs time for rectangular nozzle at NPR 2.6: (a) results for microphone **M1** in the C–D (XY) plane and (b) results for microphone **M2** in the flat plane (XZ). St at $\mathbf{R_{m1}} = 0.5$, St at $\mathbf{R_{m2}} = 0.54$.

17 March 2025 09:13:57

© Author(s) 2023

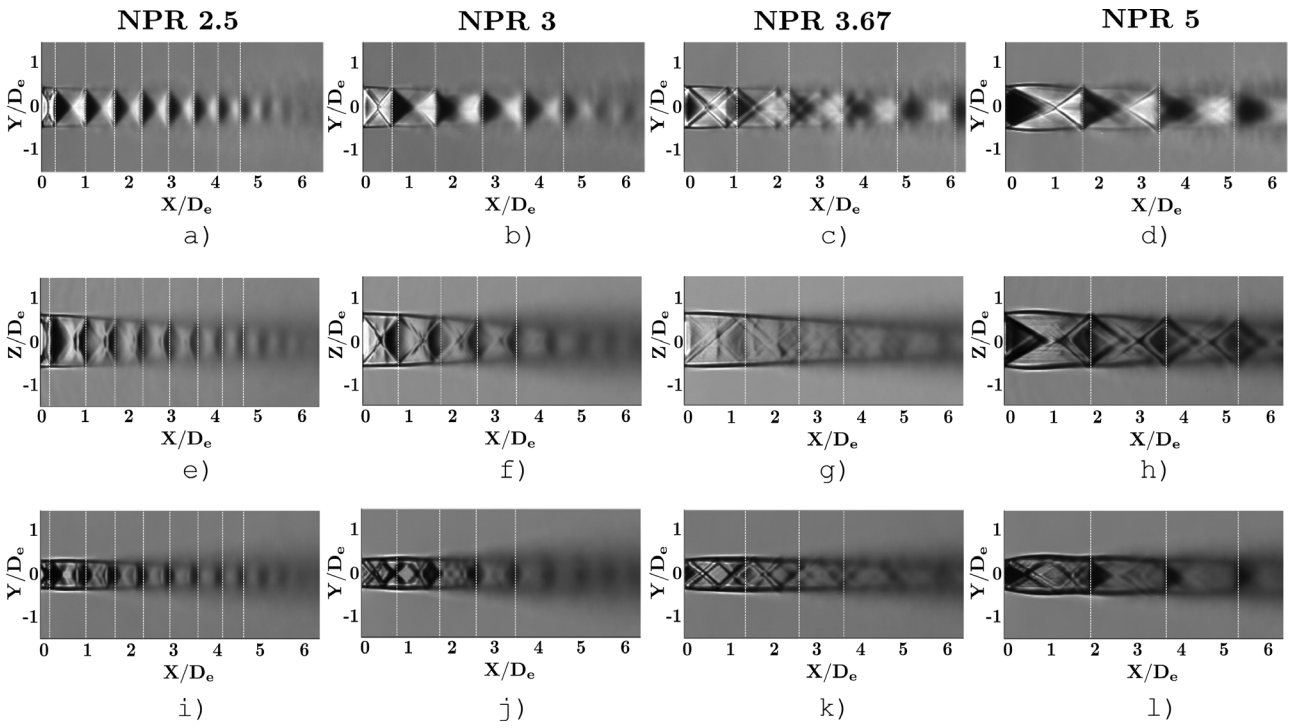


FIG. 6. Time-averaged Schlieren images: (a)–(d) circular nozzle, (e)–(h) rectangular nozzle: flat plane, and (i)–(l) rectangular nozzle: C–D plane. Each column represents the designated NPR; vertical lines represent the shock cell (pair of shock and associated expansion zone) locations.

Thus, a combination of Schlieren images and velocity profiles from particle image velocimetry (PIV) data was utilized to locate the shock inflection points on the shear layer (see Appendix C). The resulting values compared to predictions from the literature are shown in Fig. 7. The circular nozzle exhibited a notable departure from the Prandtl–Pack relation, the experimental results from Panda *et al.*[48] and the modified formulation by Gao and Li[45] at low NPRs. At higher NPR, the deviation decreased, resulting in a closer agreement between the observed and predicted values.

The initial deviation was due to the fact that the predictions and experiments mentioned above were based on purely convergent circular geometries, highlighting the effect of the secondary shock cells generated from convergent–divergent geometries. The similarity observed at higher NPRs was due to the average shock cell width being weighted by the first shock cell as a result of the limited field of view of the Schlieren system. Similar trends were documented in the computational results of Liu *et al.*[43]

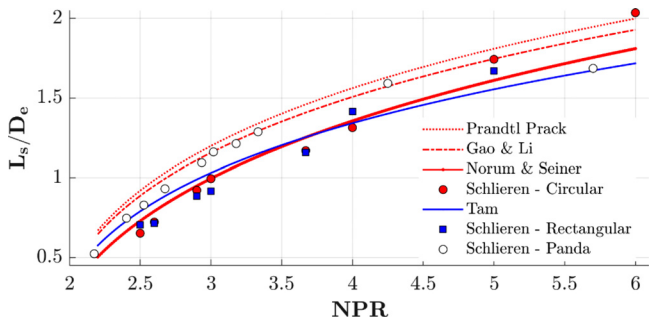


FIG. 7. NPR vs normalized average shock cell width (L_s/D_e, experiment). Curves show predictions from the literature. Red filled circle—circular, present study; red filled square—rectangular, present study; red circle—purely convergent circular nozzle from Panda.[48]

Norum and Seiner[49] proposed a formulation for shock cell width based on the model by Harper-Bourne and Fisher[50] which accounts for the secondary shock cells. This model showed better agreement with the values obtained from the experimental data. An interesting trend emerged when the results from the rectangular nozzle were added. Both configurations showed identical shock cell widths with remarkable overlap at the design condition of NPR 3.67. This suggests that the nozzle operating condition has a greater influence in the development of shock cells when compared to the geometry for jets with low AR. While the average cell width for the rectangular nozzle was close to the predictions from Tam's model[27] at low NPRs, the results from the model were underpredicted at higher NPRs. This deviation stems from the assumption of a vortex sheet formulation in the model with an enclosed shock cell structure that more closely resembles a larger AR rectangular jet, as shown in Ref. 27. Overall, the current configurations show identical trends in shock cell development. The latter part of the results focuses on the three operating conditions with high flow instabilities: NPR 2.5, NPR 2.6, and NPR 3.

Figure 8 shows the impact of these instabilities on the flow field using logarithmic intensity standard deviation contours, computed as $\log\sigma_{\partial\rho/\partial x_n}$, with each column representing one operating condition. Here, $\sigma_{\partial\rho/\partial x_n}$ is the standard deviation of temporal intensity

17 March 2025 09:13:57

© Author(s) 2023

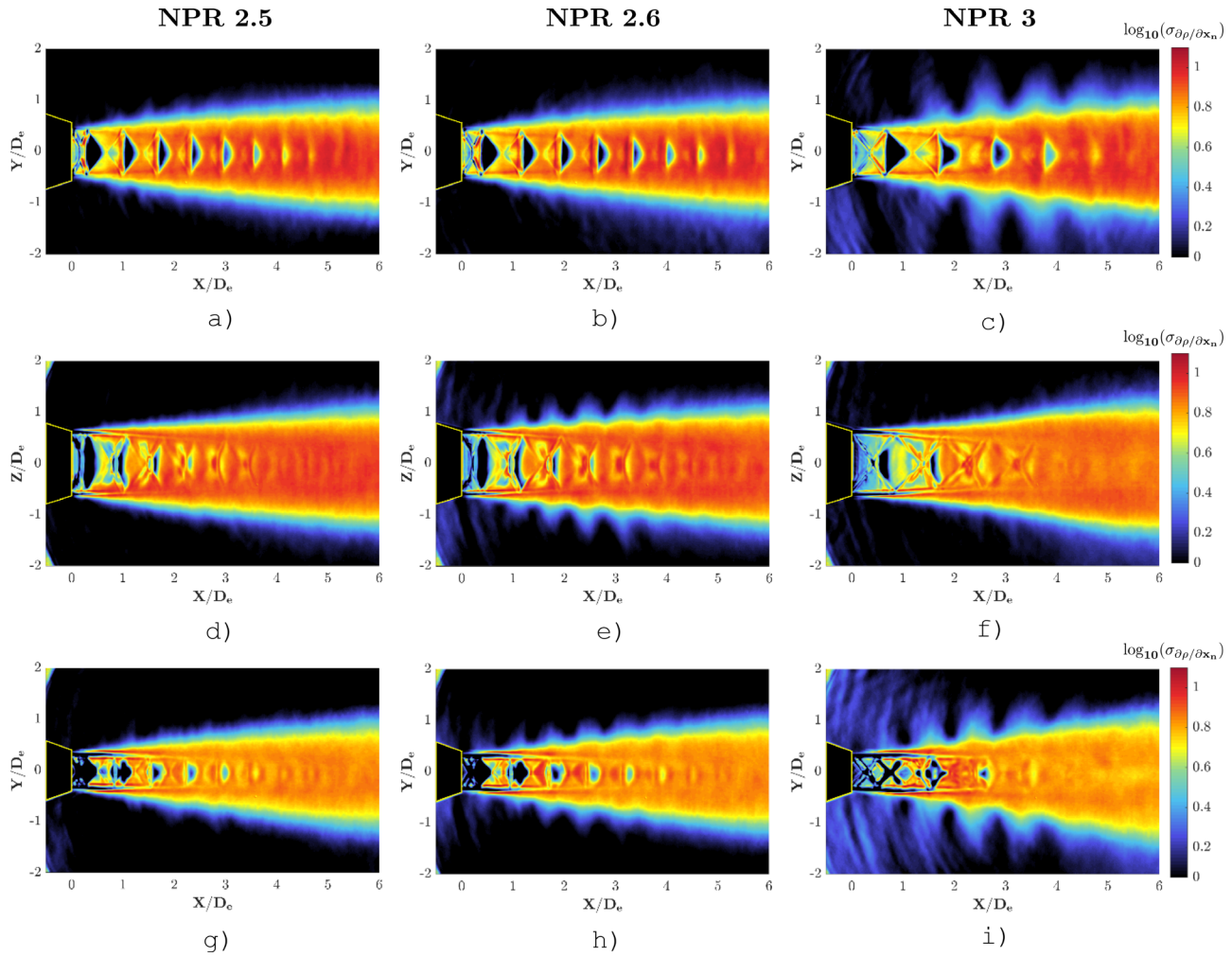


FIG. 8. Standing wave patterns visualized by contours of $\log_{10}(\sigma_{\partial\rho/\partial x_n})$. Circular nozzle: (a)–(c). Rectangular nozzle: flat plane (XZ): (d)–(f). Rectangular nozzle: C–D plane (XY): (g)–(i). Each column represents the designated NPR. Darker regions represent regions of minimal fluctuations.

fluctuations at each spatial location. These fluctuations depend on the local density gradient ($\partial\rho/\partial x_n$) along the direction x_n that is parallel to the light path (normal to the observation plane). The colormap indicates the degree of fluctuation with darker regions corresponding to minimal oscillation. The first row illustrates results for the circular nozzle, the middle row presents results for the rectangular nozzle from the flat plane (XZ), and the bottom row displays the results for the rectangular nozzle from the C–D plane (XY). Panda[11] and Edgington-Mitchell[6] showed that the interference between the upstream and downstream propagating waves at a given frequency led to the formation of standing waves in the near field of unstable jets. These waves are considered standing waves as the amplitude envelope of the interference wave is stationary, but the wave itself can manifest as a traveling wave.[6] As discussed in Sec. I, the standing wave pattern is a direct resultant of pressure fluctuations produced at the screech frequency and are correlated by Eqs. (2) and (3).

At NPR 2.5, the circular jet exhibited a diffused standing wave pattern indicating jet oscillation due to screech, as shown in Fig. 8(a). However, the rectangular nozzle only produced a faint pattern in the C–D plane (XY) as seen in Fig. 8(g), without any distinguishable pattern in the flat plane (XZ), indicating no perceivable oscillations were present in the latter orientation.

At NPR 2.6, the amplitudes of the standing wave were significantly weaker in the circular jet as depicted in Fig. 8(b), while the rectangular jet displayed a distinct wave pattern forming along both nozzle orientations, as shown in Figs. 8(e) and 8(h). This observation supports the findings from the near field acoustics results in Sec. III A, thereby visualizing the existence of concurrent instability waves that influence spanwise and streamwise fluctuations. In Fig. 8(c), a more prominent standing wave pattern can be observed for the circular jet at NPR 3 compared to previous pressure conditions. The larger radial spread of the wave peaks suggests that the amplitude of jet oscillation is greater at this condition. These findings are consistent with the results of Panda,[11] where jets oscillating in the **B** mode ($m = 1$) showed a larger radial spread of the standing wave pattern compared to those undergoing symmetric **A** mode oscillations ($m = 0$). This

17 March 2025 09:13:57

© Author(s) 2023

suggests that the circular jet issuing from the current geometry oscillates symmetrically at NPRs 2.5 and 2.6.

In contrast, the rectangular nozzle did not display any identifiable patterns in the flat plane (XZ) of the jet plume at NPR 3. However, a noticeable spread in the plume was observed across both nozzle configurations, likely due to screech flapping evident from Figs. 8(f) and 8(i). Across all the conditions, the first and second shock cells displayed consistently low levels of fluctuations. Although the shock train is a transient characteristic of supersonic jets, the system is considered quasi-steady over extended time periods due to the minimal spatial shift they undergo.

However, significant flow fluctuations such as those induced by screech tones can result in motion of the shock cells, thereby leading to higher energy levels in the shock train as seen at NPR 3 across both nozzle configurations.

C. Schlieren: Temporal analysis

Panda[11] demonstrated that tone propagation in screeching jets issuing from purely convergent nozzles occurs through two flow components: the hydrodynamic and the acoustic components. The hydrodynamic component, which is concentrated in the jet shear layer, is characterized by areas of high local pressure fluctuations and is convected downstream in the flow direction. On the other hand, the acoustic component is defined by areas of low pressure fluctuations and has two propagation directions. The upstream propagation that is driven by the interaction of the Kelvin–Helmholtz (*KH*) instabilities with the quasi-steady shock cells, and the downstream propagation that is generated by the instabilities as they traverse in the flow direction. Panda also identified the source location as the point beyond which no upstream acoustics are generated which was located between the third and fourth shock cells. Similar behavior was captured for the current circular nozzle as seen in the phase propagation contours shown in Fig. 9 (Multimedia view).

The image sequence was obtained from the temporal decomposition discussed in Sec. II C 1 at the screeching condition of NPR 3 for the circular nozzle. The contours are numbered on the order of temporal phase change (τ/T) and capture features similar to those observed by Panda. The upstream traveling acoustic component is depicted by the white arrow in Figs. 9(ii)–9(viii), while the downstream component is depicted by the orange arrow. Since the *KH* instabilities and the acoustic fluctuations generated by them share the same phase distribution, a distinction between the two was not made in these images. However, on closer examination, the downstream propagating acoustic phase front in the ambient was found leading the hydrodynamic phase front traveling along the nozzle lip line. This is expected since, at this condition, the acoustic speed of sound is greater than the convective velocity of the *KH* instabilities (u_c). This shows that the current analysis captures hydrodynamic and acoustic features. Figure 10 shows the phase distribution computed from the temporal decomposition at the respective screech frequencies for both nozzle configurations.

Symmetric phase oscillations were observed at NPR 2.5 and 2.6 for the circular nozzle, as depicted by the phase contours in Figs. 10(a) (Multimedia view) and 10(c) (Multimedia view). The instability frequency recorded for NPR 2.5 and 2.6 was $St \approx 0.61$(10 900 Hz) and $St \approx 0.56$(10 300 Hz), respectively, which corresponded to the screech frequencies observed in the far-field acoustic data. The instantaneous Schlieren images confirmed that the circular jet oscillated in the **A2** mode at these conditions (see Appendix C). At NPR 3, the azimuthal mode of the jet changed to the antisymmetric **B** mode with the jet oscillating at a frequency of $St \approx 0.37$(7100 Hz) as seen in Fig. 10(e) (Multimedia view). The origin of the screech tone was found to be between the third and fourth shock cell for all conditions based on the space time cross correlation method from Ahn *et al.*[51]

For the rectangular nozzle at NPR 2.5, the jet was found to oscillate in the antisymmetric flapping mode in the C–D plane (XY) at $St \approx 0.46$(8200 Hz) as seen in Fig. 10(b) (Multimedia view) with no periodic fluctuations observed in the spanwise direction. The axial location beyond which no upstream propagation originated from the jet was found close to $X/D_e \approx 3.6$ from the nozzle exit which placed the source close to the sixth shock cell. For NPR 3, the rectangular jet continued to fluctuate in the antisymmetric mode dominant in the C–D plane (XY) at a screech frequency of $St \approx 0.38$(7450 Hz) as seen in Fig. 10(d) (Multimedia view). The origin of the screech tone was found to be at $X/D_e \approx 3.3$ from the nozzle exit, placing the source between the third and fourth shock cells. This agrees with the results of Raman[30] (AR 4.76) and Semlitsch *et al.*[52] (AR 7).

The resolved intensity (ζ_i) profiles computed from the temporal Fourier analysis at the respective screech frequencies are shown in Fig. 11. These profiles exhibit a remarkable similarity to the acoustics distribution obtained from computations by Liu *et al.*[43] conducted for nozzles with identical design conditions. When compared to the standard deviation profiles in Fig. 8, these contours revealed a significantly pronounced standing wave pattern that extended across a substantial portion of the jet. This clarity in the pattern arises from the isolation of wave families associated with a specific frequency, thereby avoiding the amplitude attenuation caused by interference with similar wavelengths generated at other frequencies.

At NPR 2.5, the circular jet exhibited consecutive energy peaks along the lip line reaching peak intensity at $X/D_e \approx 4$ from the nozzle exit. Additionally, an acoustic component propagating upstream at a shallow azimuthal angle toward the nozzle exit was observed. This is crucial as it justifies the absence of a screech tone at this frequency in the near field results discussed in Sec. III A. The directivity angle, measured along the peaks of the standing wave from the source location between the third and fourth shock cells, was found to be $\approx 25°$ (0° upstream of the exit). This narrow angle in conjunction with the lack of significant jet-normal propagation, made the detection of the screech tone challenging in the near field measurements.

For the rectangular jet, the sinusoidal oscillations were concentrated in the C–D plane (XY) resulting in the generation of a clear standing wave pattern, with lower energy levels observed in the flat plane (XZ) as seen in Figs. 11(b) and 11(c). Peak energy concentrations were found between $3D_e$ and $4D_e$ from the nozzle exit, which closely matched the findings for the circular nozzle. However, in contrast to the circular jet, the upstream energy propagation in the rectangular nozzle was spread across a wider region. Additionally, the wavelength of the standing wave pattern was larger due to the lower instability frequency.

At NPR 3, both nozzles showed a significant increase in the energy levels as seen in Figs. 11(d)–11(f). The circular jet exhibited strong acoustic propagation emanating from the jet core up to a radial distance of $3D_e$ from the lip line driven by the antisymmetric oscillation mode ($m = 1$). The standing wave pattern consisted of four

17 March 2025 09:13:57

© Author(s) 2023

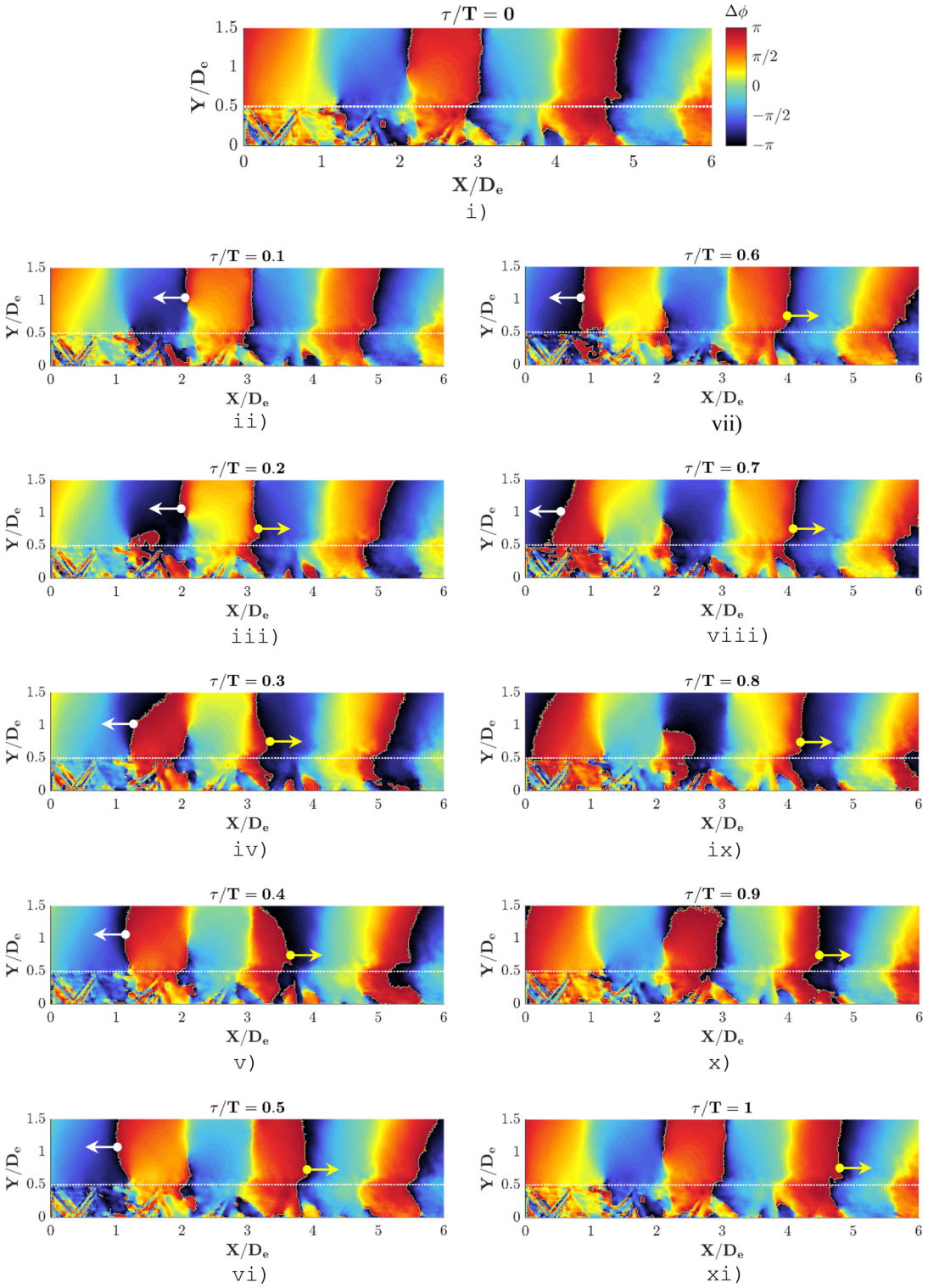


FIG. 9. Phase propagation: circular nozzle, NPR 3. The dotted line represents the nozzle lip line. White arrows: upstream propagation. Yellow arrows: downstream convection. T: time period of one screech cycle ($T = 1/f_s$), τ/T: phase time ($\tau = 0{:}0.1{:}T$). Screech frequency $St \approx 0.37$($f_s = 7100$ Hz). Flow direction: left to right. Multimedia available online.

17 March 2025 09:13:57

© Author(s) 2023

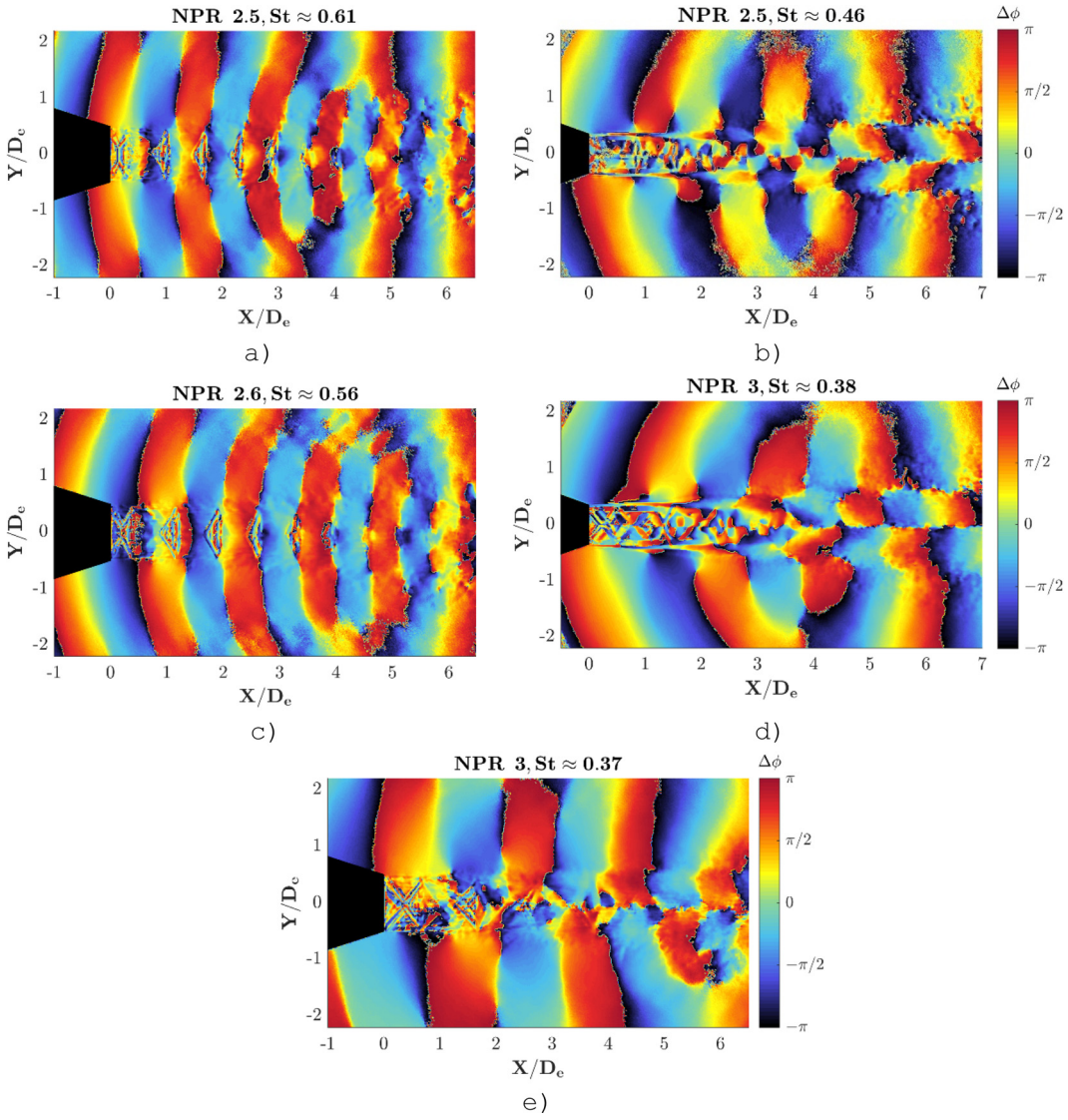


FIG. 10. Phase distribution ($\Delta\phi$) at a given operating condition and respective screech frequency. Circular nozzle—(a) NPR 2.5, (c) NPR 2.6, and (e) NPR 3. Rectangular nozzle: C–D plane (XY)—(b) NPR 2.5 and (d) NPR 3. Multimedia available online.

distinct lobes spanning $4D_e$ from the nozzle exit beyond which they merged together as seen in Fig. 11(d). In the case of the rectangular nozzle, the screech induced flapping motion in the C–D plane (XY) led to strong acoustic propagation toward the jet upstream as seen in Fig. 11(e). The intensity of this acoustic propagation was higher compared to the circular nozzle at the same condition, aligning with the findings of the near-field results. Additionally, waves originating from the jet were also observed in the flat plane (XZ) as seen in Fig. 11(e), indicating the presence of weak oscillations. Analysis of these contours revealed several noteworthy trends. First, the energy distribution started with high intensities in the ambient close to the nozzle exit and gradually shifted toward regions of local concentrations within the jet shear layers in the downstream direction. These energy levels are associated with the acoustic component close to the nozzle exit, and the coherent structures along the jet shear layer as they evolve downstream. Second, for the rectangular nozzle, significantly higher energy concentrations were observed in the C–D plane (XY) compared to the flat plane (XZ). Viswanath *et al.*[36] proposed that the development of counter-rotating vortex pairs originating from the corners of non-axisymmetric nozzles can strongly influence the formation of coherent structures. These vortices drive the fluid away from the shear layers along the smaller jet dimension toward the core and corners, resulting in higher vorticity concentrations along the central region of the wide shear layer.

Consequently, this leads to a higher concentration of energy in the wider shear layers, enhancing the energetic interactions with the shock train. The overlapping instability modes sourced from these shear layers further amplify the high-intensity fluctuations, thus

17 March 2025 09:13:57

© Author(s) 2023

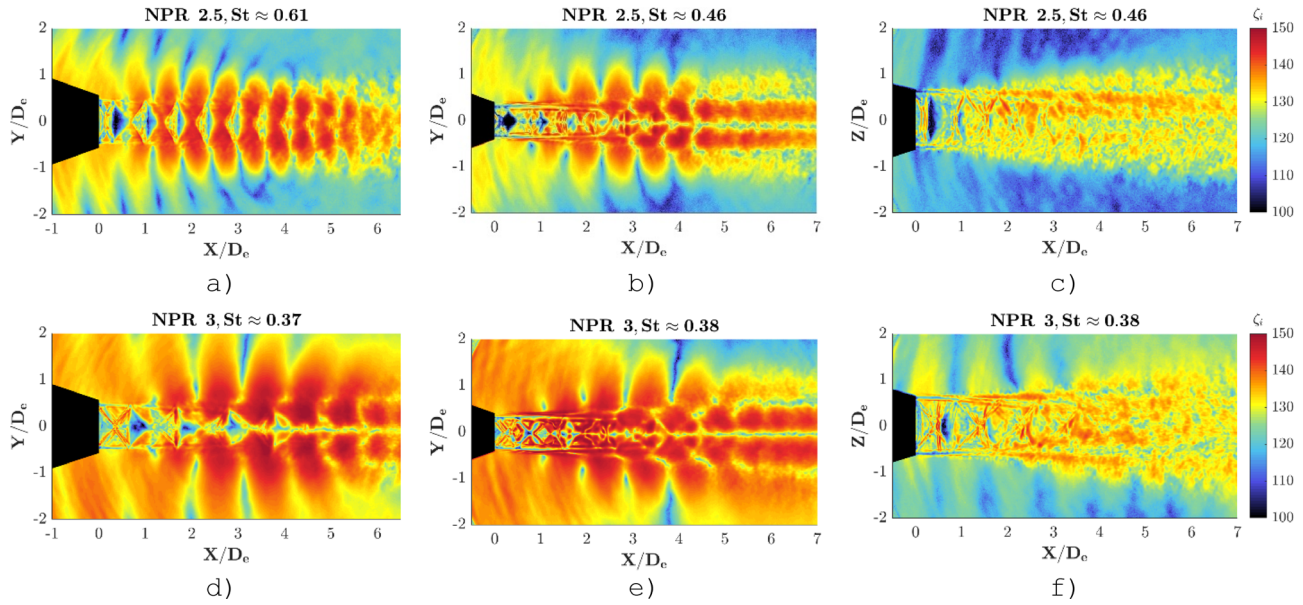


FIG. 11. Resolved intensity (ζ_i) profiles at respective screech frequencies. Top row: NPR 2.5, bottom row: NPR 3. Circular nozzle—(a) and (d). Rectangular nozzle: C–D plane (XY)—(b) and (e). Rectangular nozzle: flat plane (XZ)—(c) and (f). Note the banding of the shear layer in the rectangular nozzle due to flapping in (b) and (e).

resulting in higher energy levels in the C–D plane (XY). Finally, separation of energy bands along the shear layer was observed in the rectangular nozzle at regions beyond $X/D_e > 4$ from the nozzle exit as seen in Figs. 11(b) and 11(e). This phenomenon occurs due to the intense flapping motion exhibited by the rectangular nozzle, causing a continuous detachment of flow structures from the shear layers at the apex of each flapping wave. The cumulative effect of these separations led to valleys between regions of high energy concentration.

D. Schlieren: Spatial analysis

Before delving into the results, it is important to provide a brief explanation to fully comprehend the significance of the spatial contours presented in this section. The following discussion aims to explain the different plots shown on the contours and their significance from the point of view of wave interactions. As discussed in Sec. I, interactions between the flow constituents can be represented using their component wavenumbers given by Eq. (6), where k_{Sn} is the wavenumber of the nth shock cell

$$k = k_{KH} - k_{Sn}. \tag{16}$$

The wavenumbers corresponding to each shock cell were obtained from the temporal average of the Schlieren images.[16] Additionally, the wavenumber associated with the *KH* instabilities (the dashed yellow line) at the screech frequency (f_s) was computed using $k_{KH} = 2\pi f_s/u_c$, assuming the convective velocity relation as $u_c \approx 0.7U_j$. It is well established that the interactions of the first/optimal shock (k_{S1}, the dashed magenta line) and second/sub-optimal shock (k_{S2}, the dashed cyan line) with the *KH* instabilities have the most influence when compared to subsequent shock cells.[17] Therefore, the following discussion is centered around these two interactions. The interaction between the *KH* structures and the first shock is referred to as the optimal interaction ($k_{KH} - k_{S1}$), represented by the solid red line. The interaction with the second shock is referred to as the sub-optimal interaction ($k_{KH} - k_{S2}$), represented by the solid magenta line. The wavenumbers associated with the acoustic speed of sound ($k_{a\pm}$) are also shown for reference. As mentioned earlier, positive wavenumbers indicate waves traveling downstream, while negative wavenumbers indicate waves traveling upstream. The results of the spatial analysis are shown in Fig. 12 for the circular and rectangular nozzles for NPR 2.5 (the left column) and NPR 3 (the right column).

The decomposition was performed on the resolved intensity profiles at the respective screech frequencies. Note that the spatial wavenumber (k) is non-dimensionalized using the height of the respective nozzle configuration (D—circular, h—rectangular). The contours depict the normalized spatial Fourier energy spectra calculated along the jet axis, revealing the propagation direction of the waves across a radial span of ±2.5De from the centerline. Common trends were observed in both nozzle configurations. In both cases, distinct lobes were observed on either side of the wavenumber range, with the highest energy concentrations associated with positive wavenumbers. These regions correspond to the *KH* wave packets (k_{KH}) that propagate along the jet shear layers. The energy level associated with k_{KH} was used to re-scale the contour. These waves were also accompanied by acoustic emissions, as indicated by the presence of high-energy regions extending beyond the shear layers. On the other hand, wavenumbers associated with the first and second shock cells (k_{S1}, k_{S2}) exhibited lower energy intensities due to the relatively steady nature of the shock system, which undergoes minimal spatial fluctuations. Additionally, clear acoustic components were observed propagating in both directions, aligning with the acoustic wavenumbers $k_{a\pm}$.

For the circular nozzle operating at NPR 2.5, a distinctive energy band aligning with $k_{a\pm}$ was observed as seen in Fig. 12(a). This finding is noteworthy for several reasons. First, it suggests the presence of

17 March 2025 09:13:57

© Author(s) 2023

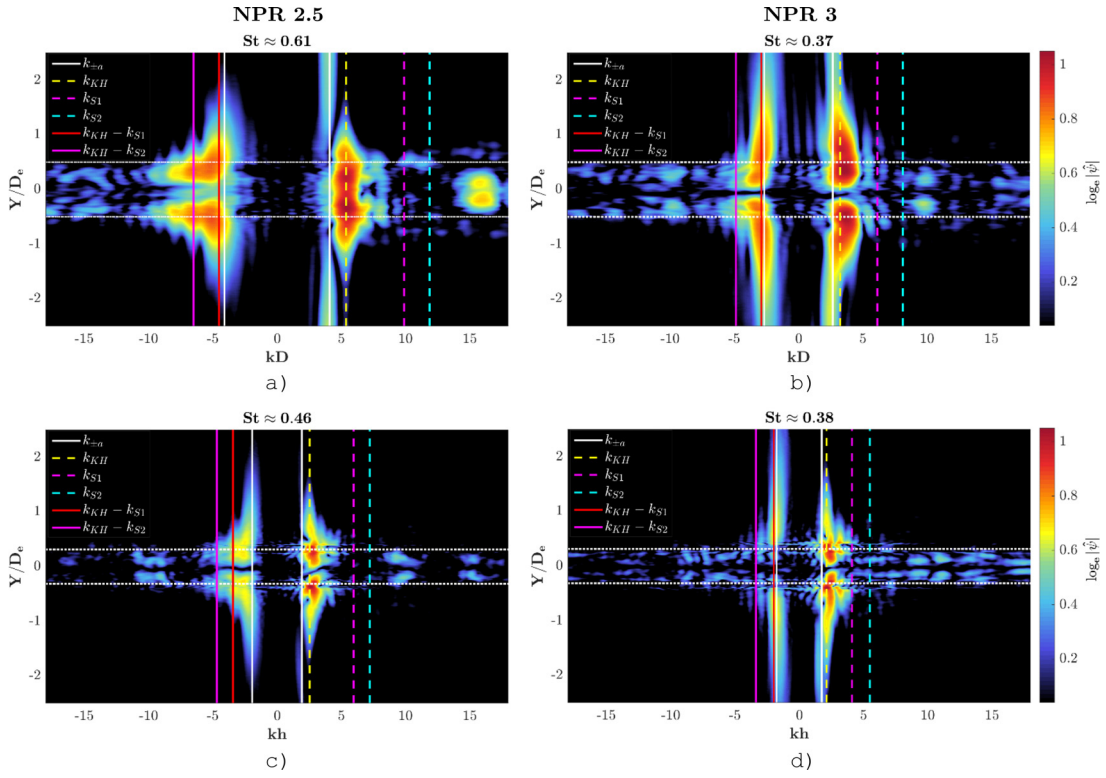


FIG. 12. Contours of energy distribution for normalized wavenumber (kh/kD) vs radial distance (Y/D$_e$). Top row: circular nozzle; bottom row: rectangular: C–D plane (XY). Left column: NPR 2.5, right column: NPR 3. White vertical line: acoustic wavenumber ($k_{\pm a}$). Yellow dashed line: KH instability wavenumber (k_{KH}). Magenta dashed line: first shock wavenumber (k_{S1}). Cyan dashed line: second shock wavenumber (k_{S2}). Red solid line: optimal interaction ($k_{KH} - k_{S1}$). Magenta solid line: sub-optimal interaction ($k_{KH} - k_{S2}$). White dotted line—nozzle lip line.

17 March 2025 09:13:57

acoustic waves that are reflected from the baseplate supporting the nozzle flange that propagate in the flow direction outside the nozzle shear layers. The intensity of this energy band increased with higher radial distance away from the centerline, indicating destructive interference near the nozzle shear layer resulting from post reflection phase inversion. Second, this observation supports the conclusion of shallow azimuthal angle discussed in Sec. III C at this condition. This pattern was not observed for other conditions/configurations in the spatial spectra.

The upstream propagation of waves within the shear layer was primarily driven by two modes, with the stronger mode resulting from the optimal interaction ($k_{KH} - k_{S1}$). This interaction gives rise to shock leakage and subsequent acoustic components that propagate into the ambient, as evidenced by the energy distribution extending beyond the shear layers up to $\pm 2D_e$. The suboptimal interaction ($k_{KH} - k_{S2}$) led to localized energy concentrations in the shear layer, which exhibited rapid dissipation within $1D_e$ from the lip line. This indicated that the G-JM is a result of the latter interaction. Interestingly, although there were multiple suboptimal peaks generated from continued interactions between the *KH* wave packets and the shock train (as seen for $k < k_{KH} - k_{S2}$), the rapid dissipation of energy within the shear layers at these wavenumbers led to minimal upstream propagation, preventing them from completing the screech resonance loop. The result that the G-JM is sourced from the suboptimal peak k_{S2} confirms that the jet oscillates in the **A2** mode, aligning with the findings of Nogueira *et al.*[20]

At NPR 3, the acoustic modes driven by the optimal interaction ($k_{KH} - k_{S1}$) exhibited significantly higher energy concentrations compared to the suboptimal interaction, as seen in Fig. 12(b). This indicated that the optimal interaction wavenumber serves as the main driver of G-JM. Therefore, in the symmetric jet mode, the G-JM is energized by interactions with the suboptimal peak (k_{S2}), while in the flapping mode, it is energized by the interaction with the optimal peak (k_{S1}). These results are consistent with the observations reported in the literature.[16]

For the rectangular geometry, the energy concentrations were significantly lower compared to the circular nozzle. This consistent trend was also observed at the harmonics of the screech frequencies, indicating the significant influence of the nozzle geometry on the development of *KH* instabilities, as discussed earlier. At NPR 2.5, the G-JM in the rectangular jet appears to be driven by the optimal interaction ($k_{KH} - k_{S1}$), as seen in Fig. 12(c). However, at NPR 3, this interaction shifted to a predominantly acoustic mode, as depicted in Fig. 12(d), with a very weak suboptimal peak. This suggests a scenario where screech closure is primarily achieved through the acoustic phase rather than the G-JM.[16] To support this observation, Schlieren images of a rectangular AR 9 SERN nozzle, studied in Semlitsch *et al.*[32] and Malla

© Author(s) 2023

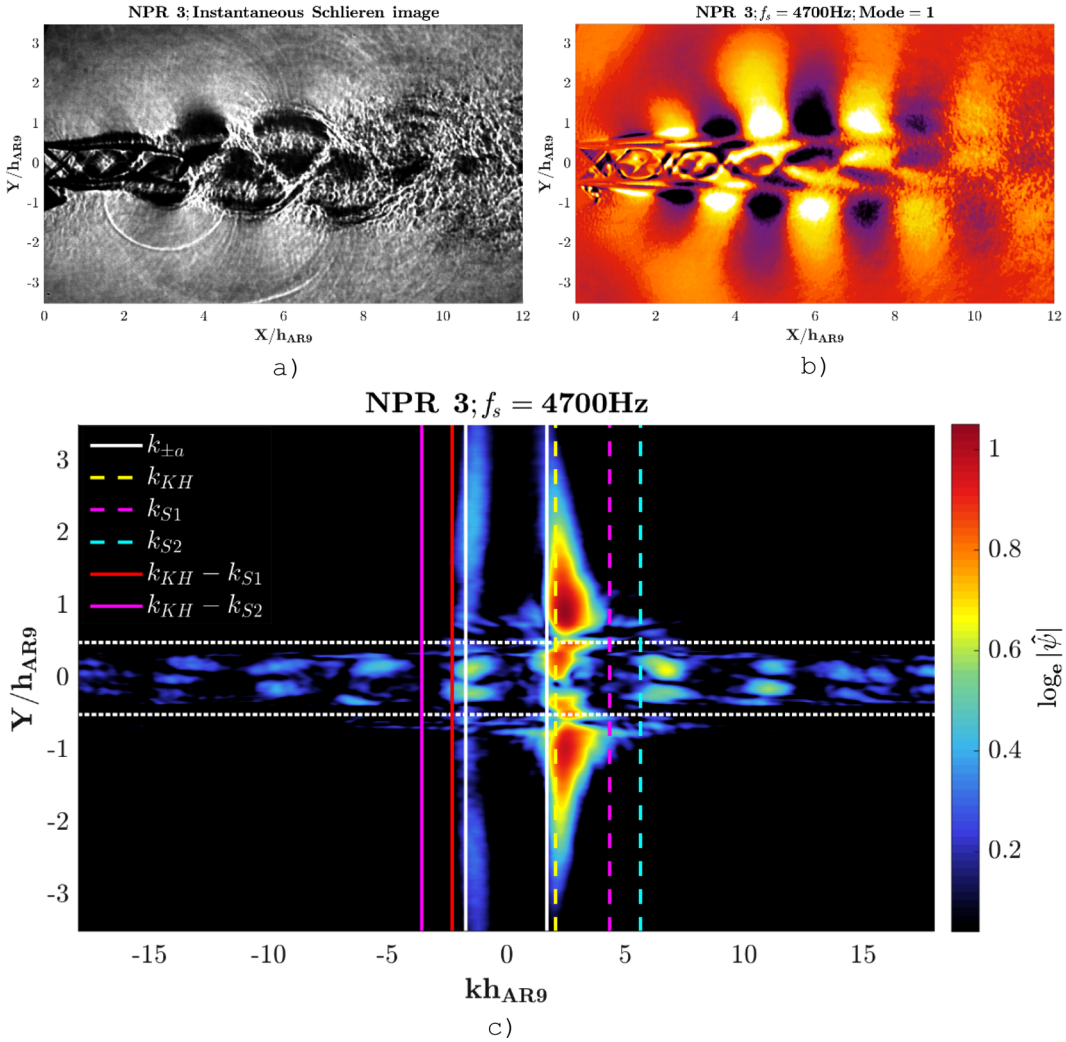


FIG. 13. (a) Instantaneous Schlieren image for an AR 9 SERN nozzle at NPR 3, (b) peak SPOD mode at fs = 4700 Hz, and (c) contours of energy distribution for normalized wavenumber (kh_{AR9}) vs radial distance (Y/h_{AR9}). Note that length scales (wavenumbers and radial distance) are normalized using height of the AR 9 nozzle (h_{AR9}). White vertical line: acoustic wavenumber ($k_{\pm a}$). Yellow dashed line: KH instability wavenumber (k_{KH}). Magenta dashed line: first shock wavenumber (k_{S1}). Cyan dashed line: second shock wavenumber (k_{S2}). Red solid line: optimal interaction ($k_{KH} - k_{S1}$). Magenta solid line: sub-optimal interaction ($k_{KH} - k_{S2}$). White dotted line: nozzle lip line. Note that k values are non-dimensionalized with nozzle height ($\mathbf{h_{AR9}}$). Multimedia available online.

et al.,[53] were analyzed. This geometry has an identical design pressure ratio of NPR 3.67 ($M_{design} = 1.5$) and undergoes strong screech driven fluctuations at NPR 3. The images were processed using the spectral proper orthogonal decomposition (SPOD) method formulated by Schmidt and Colonius.[54] An instantaneous image showing the nozzle orientation, the SPOD energy distribution associated with the primary frequency and the resulting spatial decomposition are shown in Fig. 13. The jet exhibited antisymmetric screech oscillation at NPR 3 resulting in strong acoustic emission resembling spherical shock fronts emanating from several axial locations as seen in Fig. 13(a) (Multimedia view).

For a detailed explanation of the screech generation mechanism and the resulting acoustic spectra, readers are referred to the work of Semlitsch *et al.*[32] While the nozzle had several coupled instability modes, the primary oscillation mode occurred at $f_s = 4700$ Hz with the energy distribution from the primary SPOD mode shown in Fig. 13(b) (Multimedia view). Due to the asymmetric profile of the nozzle about the midplane, the spatial energy distribution was found to be non-uniform. Higher energy concentrations were observed along the upper shear layer, driven by the flapping motion, with a peak value emerging shortly after the third shock cell at $X/h_{AR9} \approx 4.5$. This location coincided with the screech source.[32] The spatial wavenumber spectrum shown in Fig. 13(c) provided some interesting insight. The energy levels between the upstream and downstream components were significantly skewed toward the latter direction, unlike the results observed in the AR 2 nozzle. Furthermore, there was a notable increase in the

17 March 2025 09:13:57

© Author(s) 2023

energy level of the downstream component. The minimal values associated with the suboptimal interaction ($k_{KH} - k_{S2}$) indicated that a considerable amount of energy was dissipated through acoustic emission, as observed in the instantaneous image. This dissipation was driven by the optimal interaction ($k_{KH} - k_{S1}$). The absence of notable energy levels along the shear layers, coupled with the presence of energy linked to supersonic wavenumbers in the upstream direction ($0 > k > k_{a-}$), strongly indicated the presence of shock leakage.

This finding aligns with the hypothesis of Edgington-Mitchell *et al.*,[16] proposing that the triadic interactions can lead to energy redistribution altering the primary closure mechanism from G-JM to shock leakage in high AR configurations. Interestingly, the results obtained for the AR 2 nozzle at NPR 3 [Fig. 12(d)] also exhibited these characteristics indicating that shock leakage was the preferred closure mechanism for this configuration as well.

E. Multi-mode screech

As discussed in Sec. III A, the rectangular jet exhibited multi-mode screech at NPR 2.6 characterized by symmetric and antisymmetric oscillations in the jet core. Figure 14 presents the contours of resolved intensity (ζ_i) and phase distribution ($\Delta\phi$) obtained for both instability frequencies. In the case of the lower frequency $\mathbf{R_{m1}}$(St ≈ 0.5, 9100 Hz), the instability did not alter the jet behavior in the flat plane (XZ) but was dominant in the C–D plane (XY) as seen in Figs. 14(a) and 14(b). In this orientation, the jet flapping led to the formation of a standing wave pattern along the shear layers in the C–D plane (XY) similar to that observed for NPR 3.

The energy distribution also showed strong upstream propagation behind the nozzle exit. The dispersion of the energy distribution along the shear layers for $X/D_e > 3$ was also visibly driven by the flapping mode. The phase profiles associated with this frequency indicated a weak antisymmetric flapping in the flat plane (XZ) of the jet as seen in Fig. 14(c) (Multimedia view), while a clear antisymmetric phase pattern emerged in the C–D plane (XY) as seen in Fig. 14(d) (Multimedia view). The cyclic phase patterns suggested that the source of the screech tone was located between the third and fourth shock cells. For the higher frequency $\mathbf{R_{m2}}$ (St ≈ 0.54, 9900 Hz), both axes of the jet experienced simultaneous fluctuations, as evidenced by the standing wave patterns observed in Figs. 14(e) and 14(f). The intensity of these fluctuations was stronger in the flat plane (XZ), as indicated by the peaks along the shear layers and higher intensity of upstream energy propagation.

This behavior in low aspect ratio jets has not been previously documented in the literature. An intriguing feature apparent in the contours was a distinct separation between the energy lobes at $X/D_e \approx 3$ from the nozzle exit. Although visible in both orientations, it was particularly evident in the flat plane (XZ). This location marked the point beyond which upstream acoustic phase propagation was absent. A similar characteristic was observed in both the circular and the rectangular nozzle at NPR 3, close to $X/D_e = 3.5$, as shown in Figs. 11(d) and 11(e). Furthermore, the symmetric mode of oscillation induced the dispersion of the shear layer beyond $X/D_e = 5$. Figures 14(g) (Multimedia view) and 14(h) (Multimedia view) show the clear symmetric phase pattern associated with this frequency.

An intriguing finding from the cyclic phase patterns was that the source location for upstream propagation at this frequency was determined to be closer to the third shock cell. This differs from what was observed for $\mathbf{R_{m1}}$, where the source was between the third and fourth shock cells. Edgington-Mitchell *et al.*[16] investigated multi-mode behavior in purely convergent circular nozzles and concluded that each individual screech loop was driven by a unique jet mode that completes the resonance loop. The current authors believe that this could be a driving factor behind the variation in the source location observed across both frequencies.

To ascertain that the current geometry follows these trends, spatial Fourier analysis was conducted on the resolved intensity (ζ_i) plots discussed above, the results from which are shown in Fig. 15. For the lower frequency $\mathbf{R_{m1}}$, the lack of periodicity in the coherent structure generation in the flat plane (XZ) resulted in mode energies that were randomly dispersed across the wavenumber spectra, as seen Fig. 15(a). Only the acoustic noise (k_{a+}) and weak *KH* waves (k_{KH}) were discernable. In contrast, the energy spectrum for the C–D plane (XY), depicted in Fig. 15(b), displayed clear features previously observed, including the pronounced energy concentrations associated with the *KH* instabilities (k_{KH}) concentrated along the shear layers and the acoustic propagation in both upstream and downstream directions. However, unlike the pure flapping condition of NPR 3, this instability mode was considerably weaker indicated by lower overall energy levels. The energy associated with the optimal interaction ($k_{KH} - k_{S1}$) exhibited patterns resembling those of G-JM with concentrations near the jet shear layer that rapidly diminished after $Y/D_e > 1$ in the upstream direction. In contrast, the suboptimal interaction ($k_{KH} - k_{S2}$) is considerably weaker without any associated energy beyond the lip line. These findings suggest that the G-JM driving the instability at this frequency is influenced by the first shock (k_{S1}).

In the case of the higher frequency $\mathbf{R_{m2}}$, both nozzle orientations experienced symmetric oscillations, resulting in distinct energy patterns. The dominance of the symmetric mode in the flat plane (XZ) of the jet was apparent from Fig. 15(c). Clear energy bands linked to strong *KH* instabilities (k_{KH}) were observed coupled with the downstream acoustic propagation (k_{+a}). Additionally, several lower interaction modes were observed in the downstream direction driven by the superposition of various waves families.[16] The upstream acoustics were driven by the optimal jet interaction ($k_{KH} - k_{S1}$), while the G-JM was driven by the suboptimal interaction ($k_{KH} - k_{S2}$). Similar patterns in the energy distributions were observed for the C–D plane (XY) with the suboptimal interaction driving the production of G-JM. This finding is noteworthy as it demonstrates how suboptimal shock interactions can drive symmetric modes in non-axisymmetric jets, similar to its influence on the **A2** mode in circular jets. These results align well with the observations made by Edgington-Mitchell *et al.*[24] for a rectangular nozzle of identical AR. They concluded that based on the oscillation mode of the jet, the energy re-distribution resulting from the $k_{KH} - k_{S1}$ and $k_{KH} - k_{S2}$ interactions can be crucial factor in determining which shock cell influences the guided mode. From the current results, the antisymmetric modes appear to be influenced by the first shock cell (k_{S1}), while the symmetric mode appear correlated with the second shock cell (k_{S2}).

Thus, it is clear that the both instability tones in the multi-mode oscillation are driven by distinct G-JM sources. As the energy distributions were obtained from Fourier transformations, it was possible to retrieve the spatial distribution of energy associated with singular wave numbers as shown by the following equation:

$$\psi'_k(x,y) = \sum_{k_1}^{k_2} \hat{\psi}_k^{\omega}(y) e^{-ikx}, \tag{17}$$

17 March 2025 09:13:57

© Author(s) 2023

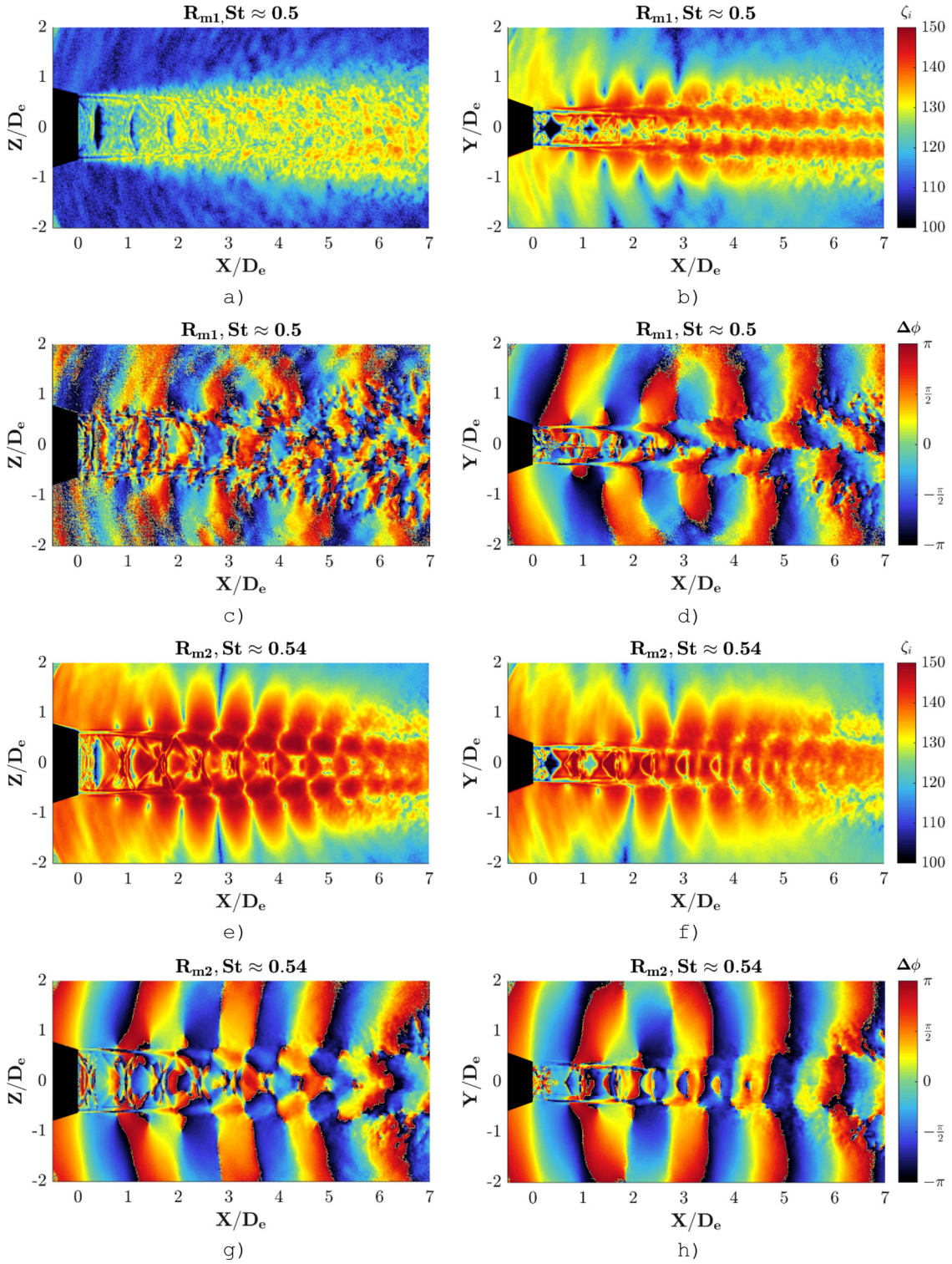


FIG. 14. Resolved intensity (ζ_i) and phase distribution for a rectangular jet at NPR 2.6: (a) flat plane (XZ), $\mathbf{R_{m1}}$ ζ_i contour, (b) C–D plane (XZ), $\mathbf{R_{m1}}$ ζ_i contour, (c) flat plane (XZ), $\mathbf{R_{m1}}$ phase contour, (d) C–D plane (XZ) $\mathbf{R_{m1}}$ phase contour, (e) flat plane (XZ) $\mathbf{R_{m2}}$ ζ_i contour, (f) C–D plane (XY) $\mathbf{R_{m2}}$ ζ_i contour, (g) flat plane (XZ) $\mathbf{R_{m2}}$ phase contour, and (h) C–D plane (XY) $\mathbf{R_{m2}}$ phase contour. Note that these instability modes occur simultaneously. Multimedia available online.

17 March 2025 09:13:57

© Author(s) 2023

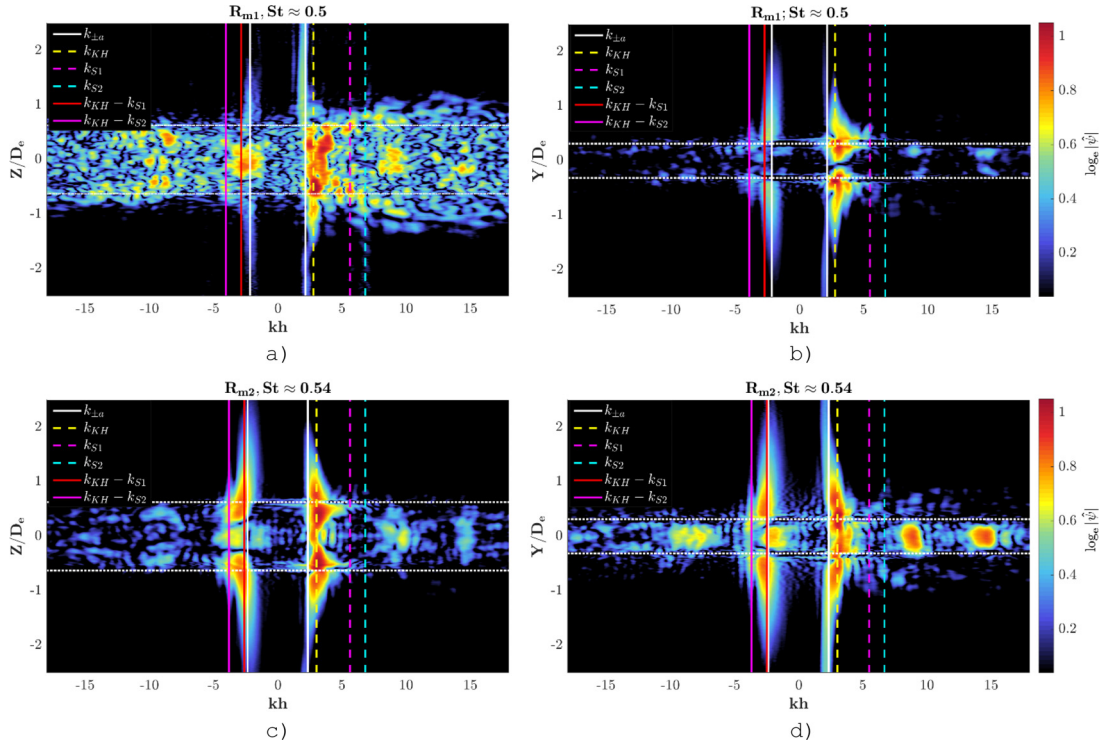


FIG. 15. Contours of energy distribution for normalized wavenumber (kh) vs radial distance (Y/D$_e$ or Z/D$_e$) for a rectangular nozzle at NPR 2.6. Top row: $\mathbf{R_{m1}}$; bottom row: $\mathbf{R_{m2}}$. Left column: flat plane (XZ). Right column: C–D plane (XY). White vertical line: acoustic wavenumber ($k_{\pm a}$). Yellow dashed line: KH instability wavenumber (k_{KH}). Magenta dashed line: first shock wavenumber (k_{S1}). Cyan dashed line: second shock wavenumber (k_{S2}). Red solid line: optimal interaction ($k_{KH} - k_{S1}$). Magenta solid line: sub-optimal interaction ($k_{KH} - k_{S2}$). White dotted line: nozzle lip line.

where $\psi'_k(x, y)$ represents the spatial distribution of energy associated with the center wavenumber k and is obtained through the inverse Fourier transform reconstructed over the wavenumber range $[k_1\ k_2]$. To achieve this, a Kaiser window with a half width of 1.5D$_e$ centered on k was employed to the domain limits. This approach is based on the techniques utilized by Edgington-Mitchell *et al.*[17] and Jeun *et al.*[55] to visualize the internal wave modes from velocity profiles. To account for the limited spatial resolution of the source images, some interpolation was applied to identify the wavenumber that is closest to the interaction wavenumbers discussed earlier. It is important to note that these modes, derived from Schlieren images, primarily serve as a qualitative representation of the energy distribution. Figure 16 illustrates the various modal energy patterns obtained for the rectangular nozzle at the multi-mode condition of NPR 2.6.

The energy distribution associated with the *KH* instability waves (k_{KH}) is depicted in the top row of contours for both instability frequencies. Figures 16(a) and 16(b) show the C–D plane (XY), while Fig. 16(c) displays the flat plane (XZ). The phase change observed in these contours reflects the oscillation mode of the jet at each frequency. These waves exhibit the highest energy levels among the interaction components as they are part of the hydrodynamic component of the flow. Additionally, ambient fluctuations driven by the instability waves as they propagate along the shear layers were visible in the contours. Although the overall convective velocity remains ≈ 0.7U$_j$ for both frequencies and nozzle orientations, the intensity of the waves differed significantly. Compared to $\mathbf{R_{m1}}$, the *KH* instability waves at $\mathbf{R_{m2}}$ exhibited higher energy levels, fueled by more energetic structures at this frequency. These levels peaked at 2.5–4D$_e$ from the nozzle exit which lies between the third and fourth shock cells. The asymmetry in the C–D plane at $\mathbf{R_{m2}}$ could result from the influence of adjacent wavenumbers due to the limited spatial resolution of the images.

Notably, the highest energy levels associated with the *KH* instabilities were observed in the flat plane (XZ), indicating the dominance of this mode in that orientation. A similar trend was observed in the wavenumber modes of upstream-propagating acoustic waves (k_{-a}) shown in Figs. 16(d)–16(f). The flat plane (XZ) at $\mathbf{R_{m2}}$ exhibited intense waves which contributed to the high noise levels observed in the near-field acoustic results at this frequency.

Interestingly, the peak locations for the acoustic waves closely aligned with those of the *KH* waves. The waves associated with G-JM (guided jet mode) are presented in the last row, represented by the interaction wavenumber k_g, as shown in the bottom row of Fig. 16. Similar to the trends observed for the *KH* instabilities and acoustic waves, the guided modes exhibited higher energy levels for $\mathbf{R_{m2}}$. The energy distribution for both frequencies exhibited the emergence of isolated lobes along the shear layer beyond X/D$_e > 2$. These lobes displayed a rapid decline in energy levels as the distance from the shear layer increased in the radial direction which is characteristic of the

17 March 2025 09:13:57

© Author(s) 2023

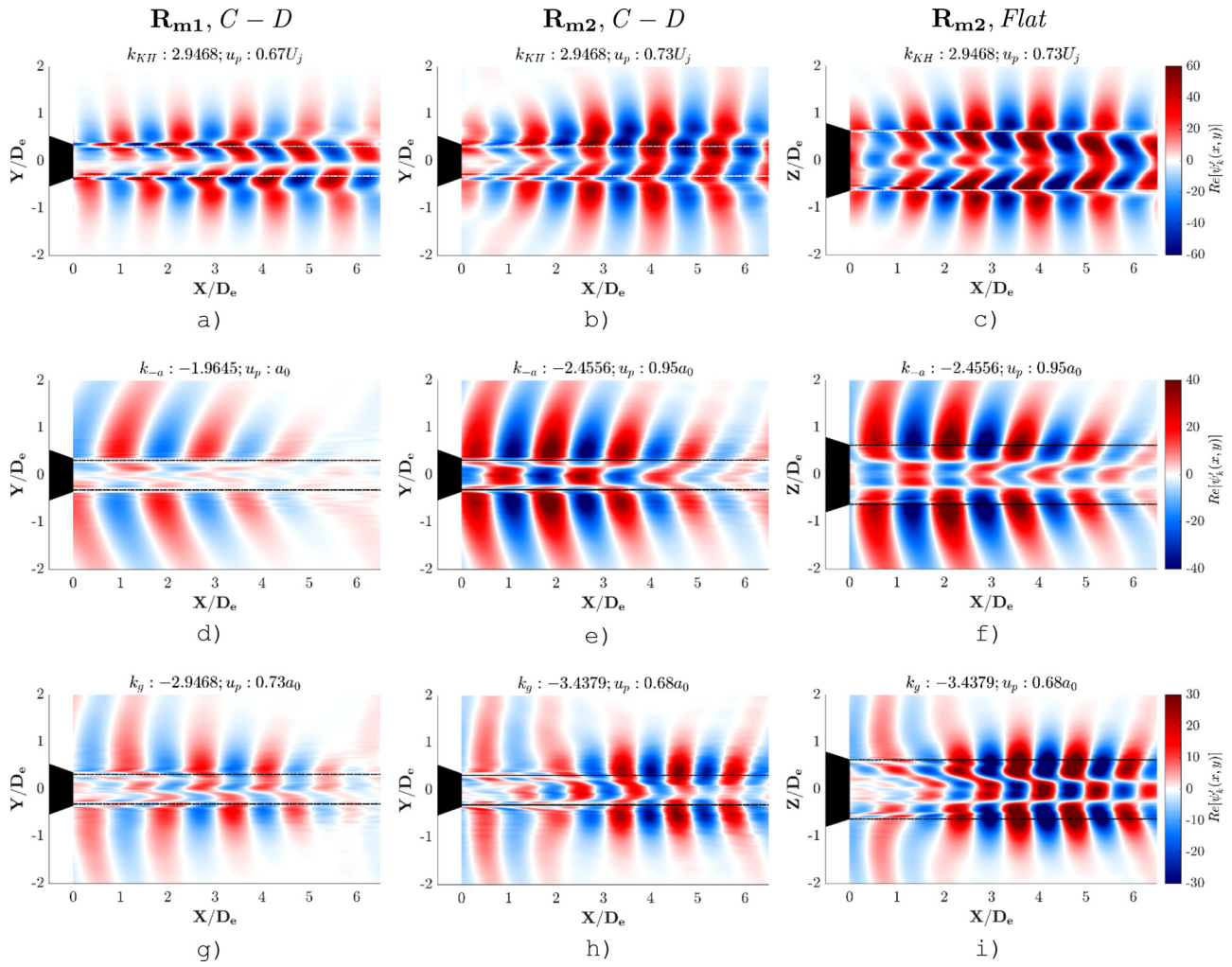


FIG. 16. Real part of reconstructed wavenumber modes for a rectangular jet at NPR 2.6. Top row: energy distribution associated with *KH* instability waves (k_{KH}). Middle row: energy distribution associated with upstream acoustic waves (k_{-a}). Bottom row: energy distribution associated with G-JM waves ($k_g = k_{KH} - k_{S1}$ *or* $k_{KH} - k_{S2}$). Also denoted is the propagation velocity (u_p) normalized by the jet exit velocity (U_j) for k_{KH} and ambient speed of sound (a_0) for k_{a-} and k_g. Note that the contour limits vary for each row based on the associated wavenumber. Left column $\mathbf{R_{m1}}$: C–D plane (XY). Middle column: $\mathbf{R_{m2}}$ C–D plane (XY). Right column: $\mathbf{R_{m2}}$ flat plane (XZ).

G-JM. Furthermore, an upstream-directed wave component was observed extending along the shear layer toward the nozzle exit, which is the resonance closure mechanism of the G-JM.

For $\mathbf{R_{m1}}$, the peak intensity occurred between the third and fourth shock cells as seen in Fig. 16(g), while for the higher frequency $\mathbf{R_{m2}}$, the peak was located closer to the third shock cell. This observation highlights a critical finding: the location of the energy peak associated with the G-JM is influenced by the optimal or sub-optimal shock interaction. In the case of the symmetric mode (driven by $k_g = k_{KH} - k_{S2}$), the energy peaks after the third shock cell, while in the antisymmetric mode (driven by $k_g = k_{KH} - k_{S1}$), it peaks closer to the fourth shock cell. This alignment with the screech tone source location is consistent with the observations made in the resolved intensity plots. Additionally, the computed propagation speed for both G-JM modes was found to be $\approx 0.7a_0$, which is in agreement with the conclusions of Shen and Tam[13] and Edgington-Mitchell *et al.*[17]

IV. CONCLUSIONS

Through the investigation of exit geometry effects on jet instabilities, several notable findings have emerged. First, in the highly overexpanded operating conditions, both the circular and rectangular nozzles exhibit some degree of screech staging. The circular nozzle transitioned from **A2** to **B** oscillation mode that was sustained up to the design condition. In contrast, the rectangular jet undergoes a mode switch from a multimode oscillation ($\hat{\mathbf{A}}$) to sustained sinusoidal fluctuations ($\hat{\mathbf{B}}$ mode) along the larger jet dimension. The analysis of resolved intensity (ζ_i) contours uncovered the presence of high amplitude standing wave patterns, which were masked by wave interactions

17 March 2025 09:13:57

© Author(s) 2023

at different frequencies along with the low angular directivity of the **A2** instability frequency in the circular jet. The higher frequency symmetric mode in **Â** mode of the rectangular nozzle displayed larger noise amplitude and propagated across all shear layers, while the lower frequency antisymmetric mode remained confined to the C–D plane (XY).

Spatial decomposition of resolved intensities provided insight into the three components resulting from triadic interactions and revealed the role of the guided jet mode (G-JM) in driving screech closure. The acoustic component of the instability was consistently influenced by the interaction of coherent structures with the first shock. However, the production mechanism of the G-JM varied depending on the azimuthal oscillation mode of the jet, with the optimal ($k_{KH} - k_{S1}$) and suboptimal ($k_{KH} - k_{S2}$) interactions playing different roles. In the case of the rectangular AR 2 nozzle, the symmetric mode of **Â** was influenced by the suboptimal peak, while the sinusoidal mode is driven by the optimal peak. Additionally, pure sinusoidal oscillations lead to diminished energy allocation to wave interactions, with acoustic propagation driven by shock leakage assuming a critical role in the feedback component that powered screech. This behavior was consistent across the AR2 and AR9 nozzles.

In conclusion, while the circular nozzle exhibited a wider range of azimuthally unstable modes, the G-JM served as the primary mode of screech closure in the symmetric **A2** mode and antisymmetric **B** mode. However, the rectangular jet revealed a more complex mechanism dictated by the dominant instability mode. Moreover, oscillation amplitude was found to alter the energy allocation resulting from triadic interactions and weaken the G-JM, thereby making acoustic propagation the primary driver of screech generation. Thus, understanding instabilities is crucial to nozzle designs to achieve predictable flow behavior and noise reduction.

ACKNOWLEDGMENTS

The authors would like to thank Dr. S. Martens and The Office of Naval Research (ONR), Washington, DC, USA for their funding and support. We express our gratitude toward Dr. D. Edgington-Mitchell, Associate Professor, Monash University, Victoria, Australia for his time and valuable comments toward development of the analysis methodology. Also acknowledged is the contribution from B. Malla, Ph.D. for allowing the use the AR 9 rectangular nozzle database.

AUTHOR DECLARATIONS

Conflict of Interest

The authors have no conflicts to disclose.

Author Contributions

Aatresh Karnam: Conceptualization (equal); Data curation (equal); Formal analysis (equal); Methodology (equal); Software (equal); Validation (equal); Visualization (equal); Writing – original draft (equal); Writing – review & editing (equal). **Mohammad Saleem:** Conceptualization (equal); Formal analysis (equal); Methodology (equal); Validation (equal); Visualization (equal); Writing – review & editing (equal). **Ephraim Gutmark:** Conceptualization (equal); Formal analysis (equal); Methodology (equal); Supervision (lead); Validation (equal); Writing – review & editing (supporting).

DATA AVAILABILITY

The data that support the findings of this study are available from the corresponding author upon reasonable request.

APPENDIX A: CIRCULAR NOZZLE SCREECH TONES

Figure 17 shows a comparison between near field and far field spectra obtained at the condition of NPR 2.5 for the circular nozzle from the azimuthal angle of $\phi = 90°$. In both cases, the axial location of the microphone coincided with the nozzle exit plane. The results were obtained from tests conducted at different time instances. A clear screech tone was detected in the far field spectrum (red) at the St ≈ 0.61(10 900 Hz), which is notably absent in the near field result. The scaled far field spectrum (blue) provides an idea of screech peak location with respect to the near field. Similar results were observed at NPR 2.6 for the circular nozzle that has a screech peak at St ≈ 0.56 (10 300 Hz, not shown).

APPENDIX B: SIGNAL ANALYSIS—RECTANGULAR NOZZLE

The following is a discussion on the results from pressure signal analysis for NPR 2.6. The phase and coherence patterns were determined through cross spectral analysis and are shown in Fig. 18. The lower frequency tone $\mathbf{R_{m1}}$(St ≈ 0.5, 9100 Hz), represented in black, showed high coherence levels in the C–D plane (XY) when analyzing microphone pressure signals from **M1** and **M3** as seen in Fig. 18(b). This suggested a strong correlation between the pressure fluctuations detected on opposite sides of the smaller jet dimension. Additionally, the phase difference of π radians between the signals indicated that the jet was undergoing sinusoidal fluctuations at this frequency. Considering the data obtained in the flat plane (XZ) from **M2** and **M4**, the coherence levels drop considerably, indicating a weaker correlation across points on either side of the spanwise direction with a phase difference of $\frac{\pi}{5}$ radians.

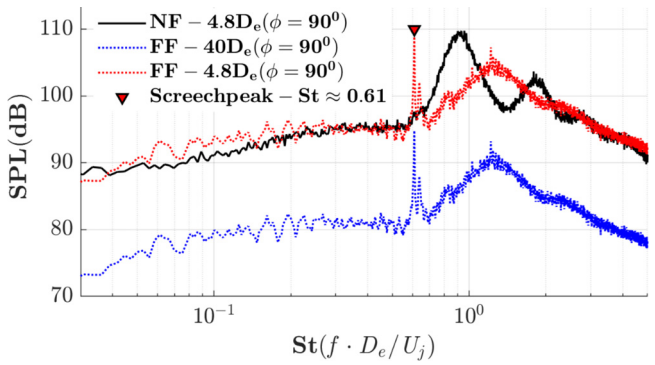


FIG. 17. Frequency spectra comparison for a circular nozzle at NPR 2.5. Microphone distance from the nozzle centerline is $4.8D_e$ for near field and $40D_e$ for far field. ϕ denotes the azimuthal angle ($\phi = 0$ located upstream of the nozzle). Dashed line—near field, red-dotted line—far field, blue-dotted line)—re-scaled far field levels using distance scaling laws.[56]

17 March 2025 09:13:57

© Author(s) 2023

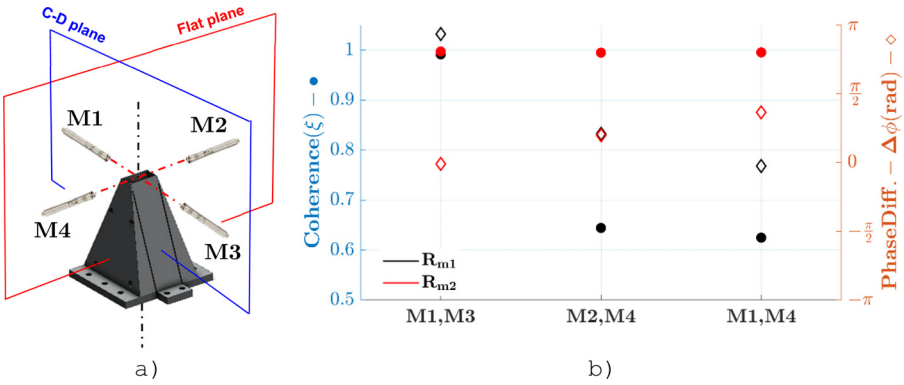


FIG. 18. Signal analysis results from near field microphones: (a) rectangular nozzle near field microphone layout (microphone axial location: nozzle exit plane), and (b) coherence (filled red circle) and phase difference (red diamond) results for instability tones R_{m1} (St ≈ 0.5) in red, and R_{m2} (St ≈ 0.54) in black.

This trend of low spatial correlation was also reflected from adjacent mics **M1** and **M4** for this frequency. The pressure fluctuations across these locations were in phase, which is expected behavior given the proximity of the jet to either microphone. The jet behavior changed considerably at the higher frequency $\mathbf{R_{m2}}$ (St ≈ 0.54, 9900 Hz), represented in red. High coherence levels were detected across both planes, implying strong similarity and synchronicity between the pressure fluctuations driven by a common source. Furthermore, the null phase in the C–D plane (XY) across microphones **M1** and **M3** indicated the jet exhibited symmetric oscillations normal to the smaller jet dimension superimposed with the asymmetric oscillations observed at $\mathbf{R_{m1}}$. In the flat plane, the phase difference switched to $\frac{\pi}{5}$ radians across microphones **M2** and **M4**, while the adjacent microphones set of **M1**, **M4** recorded a phase difference close to $\frac{\pi}{3}$ radians. These intermittent phase changes can be attributed to complex mode superposition and require further examination planned in future studies.

Another observation made during signal analysis was the modulated cross correlation pattern in Fig. 19(a) for microphones **M1**, **M3** (black plot) in the C–D plane (XY), which was likely due to the interference between the pressure fluctuations with frequencies $\mathbf{R_{m1}}$ and $\mathbf{R_{m2}}$. Conversely, the flat plane (XZ) was dominated solely by the $\mathbf{R_{m2}}$ instability tone resulting in the constant amplitude cross correlation pattern observed for microphones **M2**, **M4** (red plot) and lacked any modulation. To analyze these patterns, a set of simple sinusoidal time signals with varying angular frequencies were generated as shown below:

$$S_0 = \sin x,\ \omega = 1, \tag{B1}$$

$$S_1 = \sin\omega_1 x,\ \omega_1 = \frac{R_{m2}}{R_{m1}}, \tag{B2}$$

$$S_2 = \sin\omega_2 x,\ \omega_2 = 1.5, \tag{B3}$$

$$S_3 = \sin\omega_3 x,\ \omega_3 = 1.5. \tag{B4}$$

Cross-correlations ($\hat{C}_{xy}$) for different signal combinations with S_0 as reference were generated, as shown in Fig. 19(b). The correlation pattern $\hat{C}_{01}$ clearly resembled the results obtained from the experiment showing the effect frequency proximity has on signal correlation. Although the correlation levels observed in experimental data and control signals vary, the cyclic nature of the correlation pattern was well captured and indicated a constant cycle of constructive and destructive interference. This resulted in the development of an underlying modulation between the two frequencies. However, as the relative proximity of these frequencies decreases, this interaction cycle quickly broke down, resulting in loss of signal correlation as seen in the case of $\hat{C}_{02}$ and $\hat{C}_{03}$. The similarity between the simulated and observed results also suggested that both $\mathbf{R_{m1}}$ and $\mathbf{R_{m2}}$ are produced simultaneously. This behavior is similar to the results observed in the modulation study by Tam *et al.*[57]

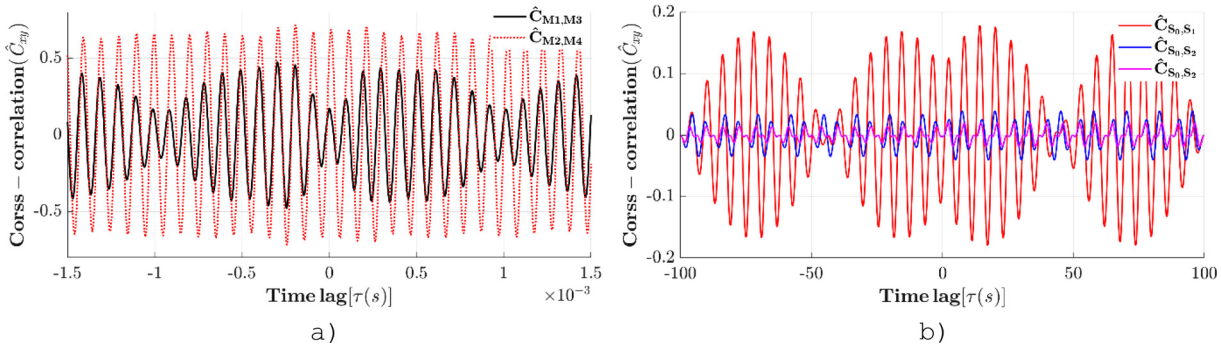


FIG. 19. Plots showing cross-correlation ($\hat{C}_{xy}$) vs time lag (τ) results: (a) experimental results from microphones in the C–D plane: **M1**, **M3** (black), and flat plane: **M2**, **M4** (red), and (b) results from simulated signal pairs, $\mathbf{S_0}$, $\mathbf{S_1}$ (red), $\mathbf{S_0}$, $\mathbf{S_2}$ (blue), $\mathbf{S_0}$, $\mathbf{S_3}$ (magenta).

17 March 2025 09:13:57

© Author(s) 2023

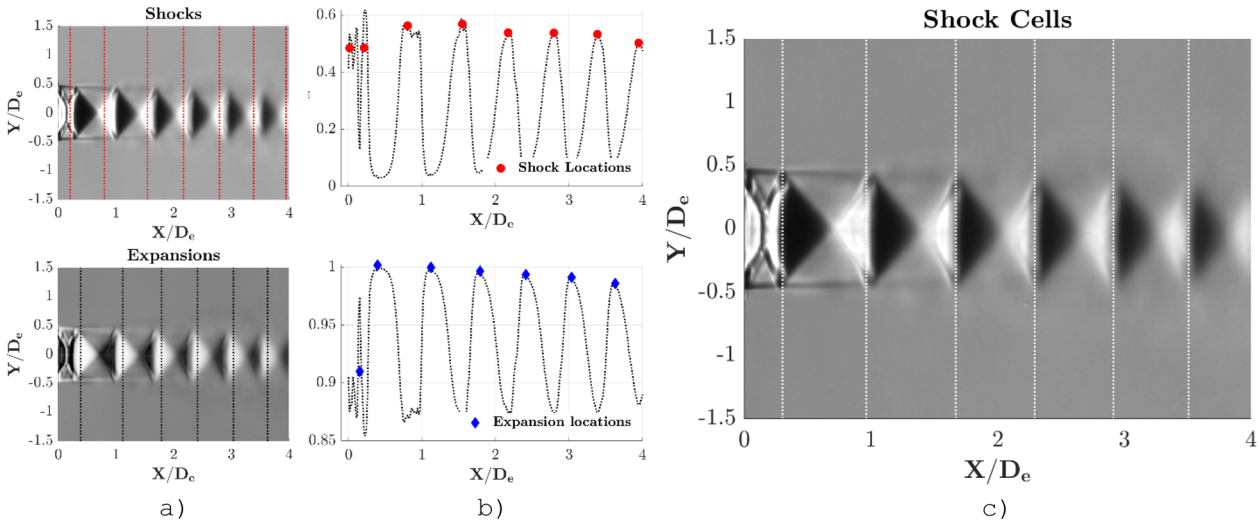


FIG. 20. Estimation of the shock cell width: (a) baseline and inverted color images used to highlight the shock (the top figure) and expansion zones (the bottom figure), (b) centerline intensity levels with peak intensity values overlaid on the top for shocks (the top figure) and expansion zones (the bottom figure), and (c) location of shock inflection points (white dotted lines) computed by averaging the spatial shock (filled red circle) and expansion (filled red diamond) locations.

APPENDIX C: SUPPLEMENTAL SCHLIEREN ANALYSIS

The shock cell width was estimated by correlating observations from Schlieren images with particle image velocimetry (PIV) data. For estimation from Schlieren data, the location of light intensities in the base image and an inverted intensity image were used as seen in Fig. 20(a) for shocks. Intensity peaks were then isolated using a shape preserving function to avoid secondary peaks generated as a result of throat shocks as seen in Fig. 20(b). The axial locations of shocks and expansions were then averaged to obtain the locations of the shock inflection points on the shear layer as seen in Fig. 20(c).

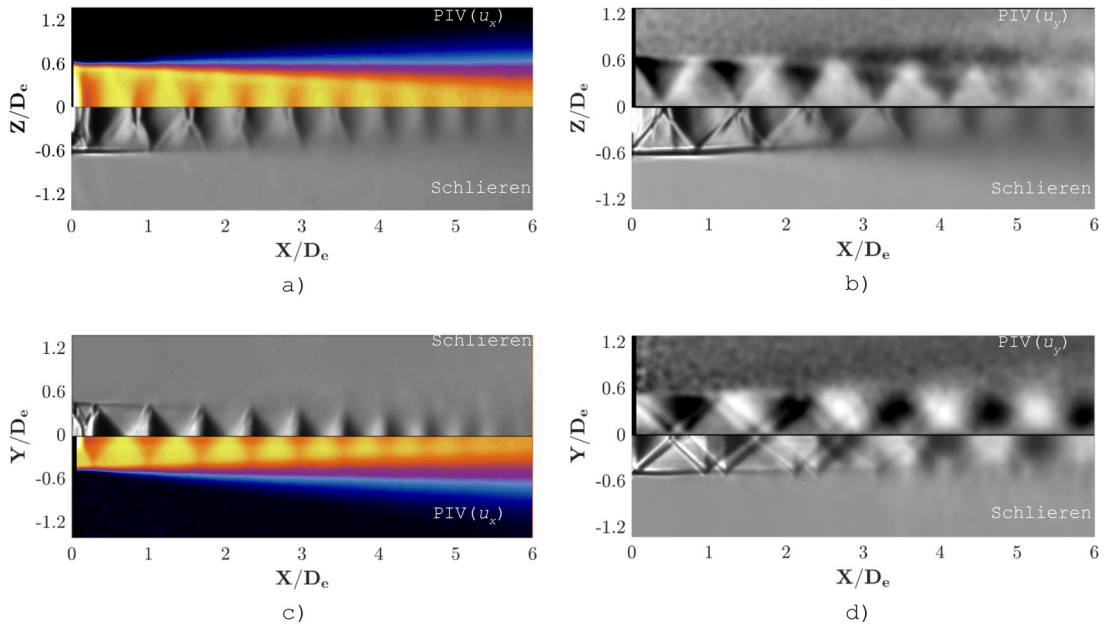


FIG. 21. Comparison of the shock structure between Schlieren and PIV data: (a) rectangular nozzle at NPR 2.5, Schlieren vs axial velocity (u_x) contour, (b) rectangular nozzle at NPR 3, Schlieren vs radial velocity (u_y) contour, (c) circular nozzle at NPR 2.5, Schlieren vs axial velocity (u_x) contour, and (d) circular nozzle at NPR 3.67, Schlieren vs radial velocity (u_x) contour. In u_y contours, dark regions represent negative velocity magnitudes, and bright regions represent positive velocity magnitudes.

17 March 2025 09:13:57

© Author(s) 2023

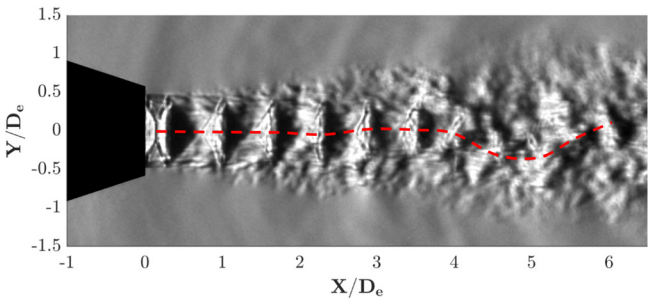


FIG. 22. Instantaneous image showing antisymmetric motion of shock cells after $X/D_e > 4$. Circular nozzle, NPR 2.5. Dashed redline shows the deviation of the jet center with respect to the geometric centerline.

To estimate the shock cell length using PIV (methodology and validation discussed in Jeun *et al.*[44]), an algorithm was utilized to correlate variations in axial velocities along the nozzle lip line with the phase/sign change noted in the radial velocity contour.

These estimations were then compared with the Schlieren images to find the closest match for each inflection point and determine the length of the shock cell. Figure 21 illustrates the excellent agreement between averaged Schlieren images and PIV velocity profiles for both jet configurations. The color scales have been adjusted to enhance the shock cell structures.

Note that in the case of NPR 3.67 in Fig. 21(d), the sensitivity of the PIV setup led to the secondary throat shock system being clearly captured in the radial velocity contour. However, the sign change from positive to negative values occurs predominantly at the inflection points generated by the exit shock system.

Powell *et al.*[9] found that jets oscillating in the **A2** symmetric instability mode were characterized by symmetric flow instabilities coupled with asymmetric oscillations in the downstream shock cells. This behavior was identified at both NPR 2.5 (seen below in Fig. 22) and at NPR 2.6 confirming that the circular jet was in the **A2** mode that these operating conditions.

REFERENCES

[1]A. Powell, "On the noise emanating from a two-dimensional jet above the critical pressure," Aeronaut. Q. **4**(2), 103–122 (1953).
[2]A. Powell, "On the mechanism of choked jet noise," Proc. Phys. Soc. B **66**(12), 1039–1056 (1953).
[3]C. K. W. Tam, "Supersonic jet noise," Annu. Rev. Fluid Mech. **27**(1), 17–43 (1995).
[4]G. Raman, "Advances in understanding supersonic jet screech: Review and perspective," Prog. Aerosp. Sci. **34**(1–2), 45–106 (1998).
[5]G. Raman, "Supersonic jet screech: half-century from Powell to the present," J. Sound Vib. **225**(3), 543–571 (1999).
[6]D. Edgington-Mitchell, "Aeroacoustic resonance and self-excitation in screeching and impinging supersonic jets—A review," Int. J. Aeroacoust. **18**(2–3), 118–188 (2019).
[7]C. K. W. Tam and H. K. Tanna, "Shock associated noise of supersonic jets from convergent-divergent nozzles," J. Sound Vib. **81**(3), 337–358 (1982).
[8]C. K. W. Tam, J. M. Seiner, and J. C. Yu, "Proposed relationship between broadband shock associated noise and screech tones," J. Sound Vib. **110**(2), 309–321 (1986).
[9]A. Powell, Y. Umeda, and R. Ishii, "Observations of the oscillation modes of choked circular jets," J. Acoust. Soc. Am. **92**(5), 2823–2836 (1992).
[10]D. Lin and A. Powell, "Symmetrical oscillation modes in choked-jet edge tones and screech from rectangular nozzles," J. Acoust. Soc. Am. **102**(2), 1235–1238 (1997).
[11]J. Panda, "An experimental investigation of screech noise generation," J. Fluid Mech. **378**, 71–96 (1999).
[12]R. Westley and J. Woolley, "The near field sound pressures of a choked jet when oscillating in the spinning mode," presented at the 2nd AIAA Aeroacoustics Conference, Hampton, VA, 24–26 1975, p. 479.
[13]H. Shen and C. K. W. Tam, "Three-dimensional numerical simulation of the jet screech phenomenon," AIAA J. **40**(1), 33–41 (2002).
[14]C. K. W. Tam and F. Q. Hu, "On the three families of instability waves of high-speed jets," J. Fluid Mech. **201**(1), 447 (1989).
[15]H. K. Tanna, "An experimental study of jet noise. II. Shock associated noise," J. Sound Vib. **50**(3), 429–444 (1977).
[16]D. Edgington-Mitchell, X. Li, N. Liu, F. He, T. Y. Wong, J. Mackenzie, and P. Nogueira, "A unifying theory of jet screech," J. Fluid Mech. **945**, A8 (2022).
[17]D. Edgington-Mitchell, T. Wang, P. Nogueira, O. Schmidt, V. Jaunet, D. Duke, P. Jordan, and A. Towne, "Waves in screeching jets," J. Fluid Mech. **913**, A7 (2021).
[18]D. Edgington-Mitchell, V. Jaunet, P. Jordan, A. Towne, J. Soria, and D. Honnery, "Upstream-travelling acoustic jet modes as a closure mechanism for screech," J. Fluid Mech. **855**, R1 (2018).
[19]M. Mancinelli, V. Jaunet, P. Jordan, and A. Towne, "Screech-tone prediction using upstream-travelling jet modes," Exp. Fluids **60**(1), 22 (2019).
[20]P. A. S. Nogueira, V. Jaunet, M. Mancinelli, P. Jordan, and D. Edgington-Mitchell, "Closure mechanism of the A1 and A2 modes in jet screech," J. Fluid Mech. **936**, A10 (2022).
[21]P. A. S. Nogueira, P. Jordan, V. Jaunet, A. V. G. Cavalieri, A. Towne, and D. Edgington-Mitchell, "Absolute instability in shock-containing jets," J. Fluid Mech. **930**, A10 (2022).
[22]C. Bogey and R. Gojon, "Feedback loop and upwind-propagating waves in ideally expanded supersonic impinging round jets," J. Fluid Mech. **823**, 562–591 (2017).
[23]R. Gojon, C. Bogey, and M. Mihaescu, "Oscillation modes in screeching jets," AIAA J. **56**(7), 2918–2924 (2018).
[24]D. M. Edgington-Mitchell, J. Beekman, and P. Nogueira, "Screech mode staging in rectangular and elliptical jets," presented at the 28th AIAA/CEAS Aeroacoustics 2022 Conference, Southampton, UK, 14-17 June 2022, AIAA Paper No. 2022–3023.
[25]R. Gojon, E. Gutmark, and M. Mihaescu, "Antisymmetric oscillation modes in rectangular screeching jets," AIAA J. **57**(8), 3422–3441 (2019).
[26]C. K. W. Tam, "On the screech tones of supersonic rectangular jets," presented at the 10th AIAA Aeroacoustics Conference, Seattle, WA, 9–11 July 1986.
[27]C. K. W. Tam, "The shock-cell structures and screech tone frequencies of rectangular and non-axisymmetric supersonic jets," J. Sound Vib. **121**(1), 135 (1988).
[28]C. K. W. Tam and A. T. Thies, "Instability of rectangular jets," J. Fluid Mech. **248**, 425–448 (1993).
[29]M. B. Alkislar, A. Krothapalli, and L. M. Lourenco, "Structure of a screeching rectangular jet: A stereoscopic particle image velocimetry study," J. Fluid Mech. **489**, 121–154 (2003).
[30]G. Raman, "Screech tones from rectangular jets with spanwise oblique shock-cell structures," J. Fluid Mech. **330**, 141–168 (1997).
[31]G. Raman and E. J. Rice, "Instability modes excited by natural screech tones in a supersonic rectangular jet," Phys. Fluids **6**(12), 3999–4008 (1994).
[32]B. Semlitsch, B. Malla, E. J. Gutmark, and M. Mihăescu, "The generation mechanism of higher screech tone harmonics in supersonic jets," J. Fluid Mech. **893**, A9 (2020).
[33]H. Suda, T. Manning, and S. Kaji, "Transition of oscillation modes of rectangular supersonic jet in screech," presented at the 15th AIAA Aeroacoustics Conference, Long Beach, CA, 25–27 October 1993.
[34]A. Towne, A. V. G. Cavalieri, P. Jordan, T. Colonius, O. Schmidt, V. Jaunet, and G. A. Brès, "Acoustic resonance in the potential core of subsonic jets," J. Fluid Mech. **825**, 1113–1152 (2017).
[35]D. Dusa, D. Speir, R. Rowe, and L. Leavitt, "Advanced technology exhaust nozzle development," presented at the 19th AIAA Joint Propulsion Conference, Seattle, WA, 27–29 June 1983.

17 March 2025 09:13:57

© Author(s) 2023

[36]K. Viswanath, R. Johnson, A. Corrigan, K. Kailasanath, P. Mora, F. Baier, and E. Gutmark, "Flow statistics and noise of ideally expanded supersonic rectangular and circular jets," AIAA J. **55**(10), 3425–3439 (2017).
[37]A. Karnam, F. Baier, and E. J. Gutmark, "Near field acoustic analysis of cold supersonic rectangular jets," presented at the AIAA Scitech 2019 Forum, San Diego, CA, 7-11 January 2019, AIAA Paper No. 2019–0809.
[38]G. S. Settles, *Schlieren and Shadowgraph Techniques* (Springer, Berlin, Heidelberg, 2001).
[39]B. Mercier, T. Castelain, and C. Bailly, "Experimental characterisation of the screech feedback loop in underexpanded round jets," J. Fluid Mech. **824**, 202–229 (2017).
[40]M. G. Berry, A. S. Magstadt, and M. N. Glauser, "Application of POD on time-resolved schlieren in supersonic multi-stream rectangular jets," Phys. Fluids **29**(2), 020706 (2017).
[41]A. Krothapalli, Y. Hsia, D. Baganoff, and K. Karamcheti, "The role of screech tones in mixing of an underexpanded rectangular jet," J. Sound Vib. **106**(1), 119–143 (1986).
[42]C. K. W. Tam, S. A. Parrish, and K. Viswanathan, "Harmonics of jet screech tones," AIAA J. **52**(11), 2471–2479 (2014).
[43]J. Liu, K. Kailasanath, R. Ramamurti, D. Munday, E. Gutmark, and R. Lohner, "Large-eddy simulations of a supersonic jet and its near-field acoustic properties," AIAA J. **47**(8), 1849–1865 (2009).
[44]J. Jeun, A. Karnam, G. Jun Wu, S. K. Lele, F. Baier, and E. J. Gutmark, "Aeroacoustics of twin rectangular jets including screech: Large-eddy simulations with experimental validation," AIAA J. **60**(11), 6340–6360 (2022).
[45]J. H. Gao and X. D. Li, "A multi-mode screech frequency prediction formula for circular supersonic jets," J. Acoust. Soc. Am. **127**(3), 1251–1257 (2010).
[46]D. Edgington-Mitchell, K. Oberleithner, D. R. Honnery, and J. Soria, "Coherent structure and sound production in the helical mode of a screeching axisymmetric jet," J. Fluid Mech. **748**, 822–847 (2014).
[47]S. Chakrabarti, D. V. Gaitonde, S. Nair Unnikrishnan, C. Stack, F. Baier, A. Karnam, and E. Gutmark, "Turbulent statistics of a hot, overexpanded rectangular jet," J. Propul. Power **38**(3), 421–436 (2022).
[48]J. Panda, G. Raman, and K. Zaman, "Underexpanded screeching jets from circular, rectangular and elliptic nozzles," presented at the 3rd AIAA/CEAS Aeroacoustics Conference, Atlanta, GA, 12–14 May 1997.
[49]T. D. Norum and J. M. Seiner, "Broadband shock noise from supersonic jets," AIAA J. **20**(1), 68–73 (1982).
[50]M. Harper-Bourne and M. J. Fisher, in *Proceedings of Noise Mechanisms* (North Atlantic Treaty Organization, Seine, France, 1973), pp. 11-1–11-13.
[51]M. Ahn, M. Mihaescu, A. Karnam, and E. Gutmark, "Large-eddy simulations of flow and aeroacoustics of twin square jets including turbulence tripping," Phys. Fluids **35**(6), 066105 (2023).
[52]B. Semlitsch, M. Mihaescu, L. Fuchs, and E. Gutmark, "Analyzing the impact of the inlet temperature on the acoustic noise production form a supersonic jet using large eddy simulations," J. Acoust. Soc. Am. **133**(5), 3264–3264 (2013).
[53]B. Malla, J. Holder, V. Anand, and E. Gutmark, "Structural excitation of SERNs during supersonic operation: A source of screech amplitude modulation," J. Fluids Struct. **107**, 103390 (2021).
[54]O. T. Schmidt and T. Colonius, "Guide to spectral proper orthogonal decomposition," AIAA J. **58**(3), 1023–1033 (2020).
[55]J. Jeun, G. J. Wu, and S. K. Lele, "A closure mechanism for screech coupling in rectangular twin jets," arXiv:2210.11567 (2022).
[56]K. Viswanathan, "Does a model-scale nozzle emit the same jet noise as a jet engine?," AIAA J. **46**(2), 336–355 (2008).
[57]C. K. Tam, M. AbuShoshah, B. Malla, and E. Gutmark, "The phenomenon of amplitude modulation of screech tones," presented at the AIAA AVIATION 2023 Forum, San Diego, CA and Online, 12–16 June 2023, AIAA Paper No. 2023–4487.

17 March 2025 09:13:57

© Author(s) 2023